Topology optimization of smart structures with embedded piezoelectric stack actuators using a composite geometry projection method

de Almeida, Breno Vincenzo; Pavanello, Renato; Langelaar, Matthijs

DOI
10.1016/j.cma.2024.117120

Publication date
2024

Document Version
Final published version

Published in
Computer Methods in Applied Mechanics and Engineering

Computer Methods in Applied Mechanics and Engineering 429 (2024) 117120

Contents lists available at ScienceDirect

Comput. Methods Appl. Mech. Engrg.

journal homepage: www.elsevier.com/locate/cma

Topology optimization of smart structures with embedded piezoelectric stack actuators using a composite geometry projection method

Breno Vincenzo de Almeida [a,b,*], Renato Pavanello [a], Matthijs Langelaar [b]

[a] Faculty of Mechanical Engineering, University of Campinas, R. Mendeleyev, 200, 13083-860, Campinas, SP, Brazil
[b] Faculty of Mechanical Engineering, Delft University of Technology, Mekelweg 2, 2628 CD, Delft, The Netherlands

ARTICLE INFO

Keywords:
Topology optimization
Piezoelectricity
Piezoelectric stack actuators
Geometry projection
Smart structures

ABSTRACT

The design of smart structures is challenging because of the integrated electromechanical modelling and optimization of actuators, sensors and load-bearing structures. To simplify the design process, it is common to decouple some of the components and physics and develop each part separately, which could lead to suboptimal systems. To improve the overall design of active structures, we propose an integrated and fully coupled design methodology for a certain class of smart structures. Specifically, this paper presents a numerical framework for the simultaneous application of density-based topology optimization of multi-material conductive compliant mechanisms and a composite multi-layered geometry-projection method for the optimization of the size, position and orientation of embedded piezoelectric stack actuators. Their electromechanical properties are represented in a continuum-based setting by an orientation- and geometry-dependent equivalent material model and their activation depends on the distribution of conductive material in the structure. Furthermore, a novel constraint on the polarization of the actuators is proposed to avoid unwanted designs that could cause their mechanical degradation. A set of numerical examples is analysed and discussed. The proposed framework exhibits promising results, with significant improvements in comparison to a benchmark problem.

1. Introduction

Smart structures, also known as active or adaptronic structures, integrate actuation, sensing and control and allow for adaptive functionalities in lightweight and low energy systems. They are characterized by the interaction of electronic and mechanical components, aiming at achieving adaptable elastomechanical properties [1]. They have a broad applicability range, such as morphing aircraft wings [2], structural health monitoring [3], nanomaterials for biomedical applications [4], among other interdisciplinary fields, combining physical, chemical and biological technologies [5].

Since active structures integrate various multidisciplinary components that have both constructive and competing interrelationships, seeking functional conformity within the system—e.g. by avoiding impedance mismatches—is a challenging aspect of their design. Hence, smart structure design inherently poses an optimization problem for which different solution strategies may be taken depending on the degree of coupling of the system components. In principle the most desirable approach is to optimize the fully coupled system, but because of the difficulty in solving the resulting large multifunctional problems, it is often necessary to

* Corresponding author at: Faculty of Mechanical Engineering, University of Campinas, R. Mendeleyev, 200, 13083-860, Campinas, SP, Brazil.
E-mail address: b135111@dac.unicamp.br (B.V. de Almeida).

https://doi.org/10.1016/j.cma.2024.117120
Received 3 April 2024; Received in revised form 21 May 2024; Accepted 2 June 2024
Available online 15 June 2024

subdivide the components and optimize each of them individually [1]. This approach may lead to suboptimal solutions from a systems perspective.

A methodical design approach to generate smart structure configurations in a multicomponent setting, capable of optimizing for actuation, sensing or energy harvesting applications, is a desirable ultimate goal. As a step in this direction, we propose a framework to design active electromechanical systems composed of piezoelectric stack actuators (PSAs) embedded within load-bearing conductive structures in a unified multiphysics setting, based on the combination of a multi-material topology optimization (TO) method and a feature-mapping method. Below various aspects of this framework are introduced and reviewed, after which we outline the contributions of this paper.

TO generates material layouts based on a set of objective and constraint functions, using computational techniques capable of taking a large amount of design variables of different degrees of complexity into account simultaneously [6]. One of the most widely used variants of TO is the density-based approach, in which 0 or 1 design variables are attributed to each element of a discretized design space, representing non-existence or existence of material, respectively. The variables are relaxed for the optimization problem to be well-posed, allowing for intermediate values, and the material properties of each element are calculated using a material interpolation law, such as the Solid Isotropic Material with Penalization (SIMP) [7]. Furthermore, multiple materials can be considered in the method by ascribing two or more design variables per element and applying different material laws [7–11]. Another widely used variant of TO is the level-set approach, in which the shape of a solid structure is determined by regions where a level-set function is greater than a given threshold, with its iso-contour representing the surface of the structure [12]. Changes in topology can be achieved by updating the level-set function, thus modifying the shape of its iso-contours, and hole nucleation can occur by incorporating other techniques, such as topological derivatives [13]. Multi-material design problems can also be considered in the method by using more than one value for the iso-contours or multiple level-set functions [14–16].

Multi-material TO has been amply applied to the design of smart structures. Sigmund [9] extended TO with multiple materials to design electrothermomechanical systems, such as an actuator or a gripper mechanism, where the input electrical voltage triggered Joule heating in the solid material causing thermal expansion. Kögl and Silva [17] proposed a novel material model for the design of piezoelectric plate and shell actuators as an extension of SIMP, adding the polarization direction of the piezoelectric material as a design variable in the optimization problem. Carbonari et al. [18] further developed the method to simultaneously optimize for the distribution of both piezoelectric and non-piezoelectric materials. Other examples of smart structure design through TO are e.g. [19–24].

Of the many components within a smart structure, actuators are the functional elements, transforming input signals into an output power, capable of generating work [1]. We focus on piezoelectric actuators, which have received significant attention over the years, due to advantages such as size compactness, large output forces, flexible design and fast frequency response [25,26]. They are composed of piezoelectric materials, which exhibit strong electromechanical coupling, generating electrical charges when subjected to an external mechanical stress and, inversely, deforming from an applied electric potential. There are several kinds of piezoelectric actuators, which can be classified according to their modes of actuation and their geometry. The actuation mode depends on the alignment between the polarization direction of the piezoelectric material and the externally applied electric field. When they are aligned, longitudinal and transverse deformations occur, while when they are perpendicular to each other, a shear mode appears. Additionally, when one end of a piezoelectric actuator is fixed, a bending mode occurs [27]. PSAs are another type of actuator, composed of piezoelectric discs or square patches stacked together in alternating polarities, sandwiched between electrodes. In comparison to other piezoelectric actuator types, they exhibit lower driving voltage, faster response times, larger blocking forces and higher eigenfrequencies [28]. For piezoelectric discs of fixed thickness, the longer the PSA, the larger its output for a given constant voltage input.

Most TO publications on piezoelectric actuators have considered single or multi-layered configurations with transverse or bending excitation modes [17–19,29–40], while very little attention has been devoted to PSAs. Recently Lai et al. [26] proposed an equivalent one-dimensional electromechanical model of a PSA based on Euler–Bernoulli beam theory, allowing for the integrated modelling and analysis of piezo-actuated compliant mechanisms. The model was developed for the dynamic stiffness matrix method [41], so incorporating it into a density-based TO framework is not straightforward. Instead, we propose a novel continuum-based model via an equivalent piezoelectric material that has geometry dependent properties, calculated based on the length and orientation of the PSA during the design procedure.

PSAs are typically available in regular geometric shapes, and this property should be considered when optimizing a smart structure with embedded PSAs. This is not straightforward in the aforementioned TO methods. A class of methods that can do so is broadly called feature-mapping methods [42]. Wang et al. [33] performed TO of compliant smart structures with embedded piezoelectric actuators in a hybrid level-set and nodal density-based approach. Yang et al. [36] optimized the topology of piezoelectric composites with integrated actuators, geometrically modelled using the Finite Circle Method. Recently Wang et al. [39] applied the method of Moving Morphable Components (MMC) and minimum length scale control to obtain optimized compliant mechanisms and actuators. In this work, we apply the geometry projection method [43] to optimize the sizes and placements of the PSAs. With this method, the lengths and orientations of the PSAs are explicitly known, which synergizes with the proposed equivalent piezoelectric material model mentioned above.

A PSA should only connect to a load-bearing structure through its ends and bending modes should not occur, since this could cause delamination between the discs within the PSA and breakage [5,44]. To take these physical considerations into account, the PSA is modelled using geometry-projection via a combination of an active piezoelectric layer, a void layer encapsulating its sides and an electrode layer at its extremities. Therefore, a composite multi-layered adaptation of the geometry-projection method is developed

to model the PSA, with distinct material properties being attributed to fixed subregions within its geometry. Furthermore, a novel polarization constraint is proposed to avoid designs where the PSA acts under tension, which can cause its mechanical degradation.

The proposed framework models the electrical connections between electrodes and actuators explicitly, to obtain more realistic designs, which requires strongly-coupled electromechanical equations to model the load-bearing regions of the design. This is achieved by allowing for a monolithic interpolation between non-conductive (void and solid dielectric) and conductive (solid) materials using SIMP and therefore the material interpolation laws require special attention. Yoon and Sigmund [45] proposed a nonlinear continuum-based formulation valid for general media consisting of ideal insulators and conductors for the design of electrostatic systems actuated by Coulomb's forces; they coined a generalized permittivity that is equal to the permittivity of air in void regions, but equal to a very large number in solid regions. Chen et al. [46] used a simplified model for energy harvesting applications by considering the coupled linear equations of piezoelectric media and directly attributing large permittivity values to conductive media. He et al. [47] applied a further simplification by neglecting the permittivity of conductive materials altogether, which avoids numerical issues related to the usage of large values in the analyses, despite compromising its accuracy. In this work we take a similar approach as [46] and perform a brief investigation on the effect of the permittivity value of the conductive material on the optimization process.

The main contributions of this work are fourfold: 1) introduction of a continuum equivalent material model for PSAs; 2) a composite multi-layered geometry projection method; 3) its simultaneous application to the TO of the load-bearing part of the smart structure in a multiphysics multi-material dielectric–conductive design; and 4) a polarization constraint for PSAs. Together, these advances allow for TO of PSA-driven smart structures considering mechanical and electrical functionality, with realistic and controlled PSA geometries. In this work, two-dimensional (2D) plane strain hypothesis was considered given the planar target applications and to simplify the analysis procedure, however most of the developments can be trivially extended to three dimensions (3D). Where relevant, remarks regarding the extension to 3D will be included below.

The paper is divided as follows. In Section 2 the formulation of the equivalent PSA material is derived, the piezoelectric finite element discretization is given and the composite multi-layered geometry-projection method used to geometrically model the PSA is introduced. Section 3 presents the three-phase SIMP interpolation used to interpolate between void, solid dielectric and solid conductive materials in the load-bearing region of the structure as well as the complete formulation combining it with the composite geometry-projection method representing the PSAs. The optimization problem is stated in Section 4 with the objective function, the constraints, sensitivity analysis and details on the solution process. Results are presented and discussed in Sections 5 and 6 concludes the paper.

2. Modelling

An illustration of how the smart structure is modelled can be seen in Fig. 1. The design domain is represented by the domain Ω, which is conceptually divided in two independent ways: a geometric set and a material set, shown in Figs. 1(b) and 1(c), respectively. In the geometric set, actuators are defined by the domain Ω_{A}, which can be written as the union of all individual actuator domains $\Omega_{\mathrm{A}} = \bigcup_i \Omega_{\mathrm{A}_i}$. The full domain thus contains Ω_{A} and its complement $\Omega_{\mathrm{A}}^{\mathrm{c}}$. The material of each Ω_{A_i} has its own equivalent PSA property, which is derived in Section 2.1. Next, the discretization methodology using the Finite Element Method (FEM) is given in Section 2.2. Finally, Section 2.3 shows how geometry projection is used to map the geometric variables that describe the PSAs to element-wise pseudo-densities, as well as the FEM stiffness matrices associated to each actuator Ω_{A_i}. The material set describes the load bearing structure, containing void Ω_{V}, dielectric Ω_{D} and conductive Ω_{C} regions and is introduced in Section 3.

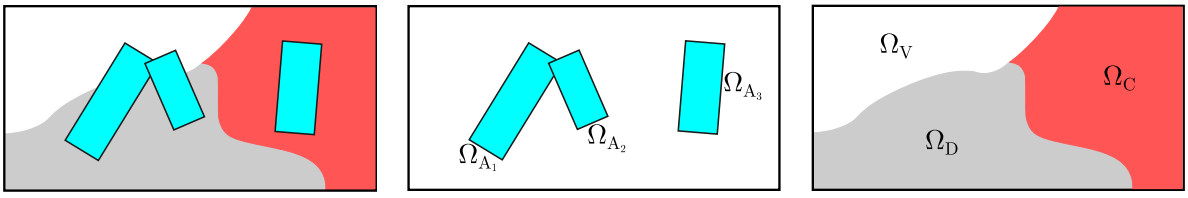

(a) Full design domain Ω.

(b) Geometric set. The actuator regions Ω_{A_i} are described using geometry projection.

(c) Material set. The void Ω_{V}, dielectric Ω_{D} and conductive Ω_{C} regions are interpolated using pseudo-densities.

Fig. 1. Conceptual division of the design domain. White is void, grey is dielectric material and red is conductive material. The rectangular blue regions are stack actuators. (For interpretation of the references to colour in this figure legend, the reader is referred to the web version of this article.)

2.1. Piezoelectric stack actuator material model

A classical piezoelectric stack actuator (PSA) is composed of multiple thin piezoelectric discs, stacked together with alternating polarization directions, with electrodes between them. Fig. 2 illustrates the actuator. Compared to a monolithic piezoelectric cylinder with the same volume, for a given voltage difference between its ends, the PSA deforms significantly more than the monolithic cylinder.

Typically, the thickness of the piezoelectric discs ranges from 50 to 100 μm [48]. Since the PSAs are embedded in the topology, as opposed to considering plate-like actuators, with out-of-plane electrical excitation [39], the behaviour of a PSA has to be taken

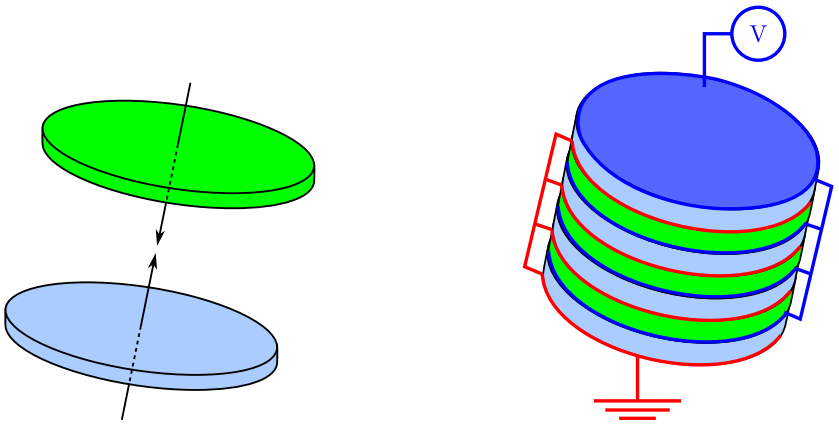

(a) Two thin piezoelectric discs with inverted polarization directions.

(b) Piezoelectric stack actuator (PSA).

Fig. 2. Illustration of a classical PSA. Blue indicates upward and green indicates downward polarization directions. (For interpretation of the references to colour in this figure legend, the reader is referred to the web version of this article.)

into account in the model. Although this could be performed in a Finite Element setting by considering a mesh fine enough to capture the different piezoelectric discs and electrodes, this is computationally expensive. Instead, equivalent piezoelectric material properties are proposed to model the behaviour of the PSA. It is assumed that the discs are perfectly bonded to each other.

To obtain the equivalent properties of the PSA, we write the constitutive equations of piezoelectric media in the strain-charge form, or d-form, shown in Eq. (1), in Voigt notation. Note that by the IEEE standard for piezoelectricity, the 3rd dimension is considered to be the polarization direction [49].

$$\begin{aligned} \boldsymbol{S} &= \boldsymbol{s}^{\mathrm{E}}\boldsymbol{T} + \boldsymbol{d}^{\mathrm{T}}\boldsymbol{E} \\ \boldsymbol{D} &= \boldsymbol{d}\,\boldsymbol{T} + \boldsymbol{\varepsilon}^{\mathrm{T}}\boldsymbol{E} \end{aligned} \tag{1}$$

$\boldsymbol{T}$, $\boldsymbol{S}$, $\boldsymbol{D}$ and $\boldsymbol{E}$ are the stress, strain, dielectric displacement and electric field vectors, respectively. $\boldsymbol{s}^{\mathrm{E}}$ is the compliance matrix evaluated at constant electric field, $\boldsymbol{d}$ is the piezoelectric coupling matrix and $\boldsymbol{\varepsilon}^{\mathrm{T}}$ is the dielectric permittivity evaluated at constant stress.

Now consider Eq. (1) for a one-dimensional (1D) model, as illustrated in Fig. 3. The polarization direction of the discs of thickness t_{d} is in the x_3 direction. Since neither stresses nor charges are applied to its ends, other than a voltage of value ϕ, there are no stresses in the PSA. The electric field in the x_3 direction for each disc may be written as $E_3 = -\frac{\phi}{t_{\mathrm{d}}}$. The total length L of the PSA is equal to t_{d} times the number of discs n, i.e. $L = n\,t_{\mathrm{d}}$. Thus, $E_3 = -n\frac{\phi}{L}$. Then from the first equation in Eq. (1), we have that the strain in the PSA is constant and equal to

$$S_{33} = -n d_{33}\frac{\phi}{L} \tag{2}$$

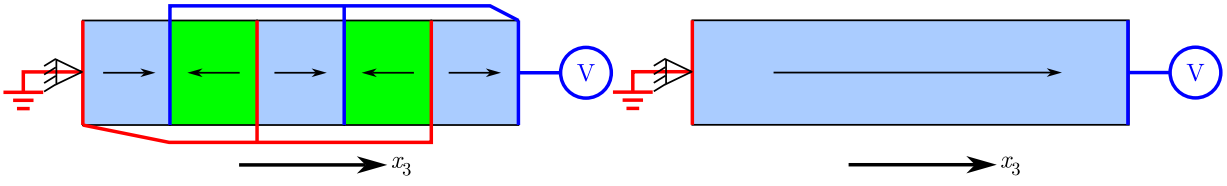

(a) Full model.

(b) Equivalent model.

Fig. 3. 1D model of a PSA.

Therefore, the 1D PSA of length L may be written as consisting of an equivalent monolithic piezoelectric material with an equivalent property $d_{33_{\mathrm{PSA}}} = n\,d_{33}$, with a constant electric field $E_3 = -\frac{\phi}{L}$ [48].

Now, regarding the purely electrical properties of the material, the capacitance C_{disc} of each disc can be expressed as

$$C_{\mathrm{disc}} = \frac{\varepsilon_{33}^{\mathrm{T}} A_{\mathrm{d}}}{t_{\mathrm{d}}} \tag{3}$$

where A_{d} is the surface area of the discs, which is equal to the cross section area of the PSA.

Since the PSA is a parallel connection of n discs, then $C_{\text{PSA}} = n\,C_{\text{disc}}$. Using this, Eq. (3) and $L = n\,t_{\text{d}}$ we have that

$$C_{\text{PSA}} = \frac{n^2 \varepsilon_{33}^{\text{T}} A_{\text{d}}}{L} \tag{4}$$

Therefore the equivalent $\varepsilon_{33}^{\text{T}}$ property of the PSA may be written as $\varepsilon_{33_{\text{PSA}}}^{\text{T}} = n^2 \varepsilon_{33}^{\text{T}}$ [48]. In summary, a 1D PSA of n piezoelectric discs may be modelled as being composed of a single equivalent piezoelectric material with properties shown below, which is illustrated in Fig. 3(b).

$$\begin{aligned} d_{33_{\text{PSA}}} &= n\,d_{33} \\ \varepsilon_{33_{\text{PSA}}}^{\text{T}} &= n^2 \varepsilon_{33}^{\text{T}} \end{aligned} \tag{5}$$

In order to find the equivalent PSA properties for a 2D case considering plane strain hypothesis, the equivalent 2D strain-charge constitutive equations are required. However, this form of the equations cannot be immediately obtained from the 3D case of Eq. (1) by just ignoring the out-of-plane dimension. Instead, the equations are firstly written in the stress-charge form, or e-form, shown in Eq. (6), and then changed to the strain-charge form, as in Eq. (1).

$$\begin{aligned} \boldsymbol{T} &= \boldsymbol{c}^{\text{E}} \boldsymbol{S} - \boldsymbol{e}^{\top} \boldsymbol{E} \\ \boldsymbol{D} &= \boldsymbol{e}\,\boldsymbol{S} + \boldsymbol{\varepsilon}^{\text{S}} \boldsymbol{E} \end{aligned} \tag{6}$$

where $\boldsymbol{c}^{\text{E}}$ is the elasticity matrix evaluated at constant electric field, $\boldsymbol{\varepsilon}^{\text{S}}$ is the permittivity matrix evaluated at constant strain and $\boldsymbol{e}$ is the piezoelectric coupling matrix in this form.

To change between the two forms of the constitutive equations, the following relationships are applied:

$$\begin{aligned} \boldsymbol{s}^{\text{E}} &= \boldsymbol{c}^{\text{E}^{-1}} \\ \boldsymbol{d} &= \boldsymbol{e}\,\boldsymbol{s}^{\text{E}} \\ \boldsymbol{\varepsilon}^{\text{T}} &= \boldsymbol{\varepsilon}^{\text{S}} + \boldsymbol{e}\,\boldsymbol{d}^{\top} \end{aligned} \tag{7}$$

Considering 2D plane strain hypothesis, with direction x_2 as the out-of-plane direction, and that only piezoelectric materials of crystalline structure class 4*mm* are taken into account, which are transversely isotropic [49], Eq. (6) may be written as

$$\begin{aligned} \begin{Bmatrix} T_{11} \\ T_{33} \\ T_{13} \end{Bmatrix} &= \begin{bmatrix} c_{11}^{\text{E}} & c_{13}^{\text{E}} & \\ c_{13}^{\text{E}} & c_{33}^{\text{E}} & \\ & & c_{55}^{\text{E}} \end{bmatrix} \begin{Bmatrix} S_{11} \\ S_{33} \\ S_{13} \end{Bmatrix} - \begin{bmatrix} & e_{31} \\ & e_{33} \\ e_{15} & \end{bmatrix} \begin{Bmatrix} E_1 \\ E_3 \end{Bmatrix} \\ \begin{Bmatrix} D_1 \\ D_3 \end{Bmatrix} &= \begin{bmatrix} & & e_{15} \\ e_{31} & e_{33} & \end{bmatrix} \begin{Bmatrix} S_{11} \\ S_{33} \\ S_{13} \end{Bmatrix} + \begin{bmatrix} \varepsilon_{11}^{\text{S}} & \\ & \varepsilon_{33}^{\text{S}} \end{bmatrix} \begin{Bmatrix} E_1 \\ E_3 \end{Bmatrix} \end{aligned} \tag{8}$$

Common piezoelectric ceramic materials such as barium titanate ($BaTiO_3$) and lead zirconate titanate (PZT) are examples of such class of materials. Substituting Eq. (7) into Eq. (8), the constitutive properties in the strain-charge form under plane strain hypothesis are finally obtained:

$$\begin{aligned} \begin{Bmatrix} S_{11} \\ S_{33} \\ S_{13} \end{Bmatrix} &= \begin{bmatrix} s_{11}^{\text{E}} & s_{13}^{\text{E}} & \\ s_{13}^{\text{E}} & s_{33}^{\text{E}} & \\ & & s_{55}^{\text{E}} \end{bmatrix} \begin{Bmatrix} T_{11} \\ T_{33} \\ T_{13} \end{Bmatrix} + \begin{bmatrix} & d_{31} \\ & d_{33} \\ d_{15} & \end{bmatrix} \begin{Bmatrix} E_1 \\ E_3 \end{Bmatrix} \\ \begin{Bmatrix} D_1 \\ D_3 \end{Bmatrix} &= \begin{bmatrix} & & d_{15} \\ d_{31} & d_{33} & \end{bmatrix} \begin{Bmatrix} T_{11} \\ T_{33} \\ T_{13} \end{Bmatrix} + \begin{bmatrix} \varepsilon_{11}^{\text{T}} & \\ & \varepsilon_{33}^{\text{T}} \end{bmatrix} \begin{Bmatrix} E_1 \\ E_3 \end{Bmatrix} \end{aligned} \tag{9}$$

Now consider the illustrations shown in Fig. 4 of a 2D PSA model. The actuation direction of the PSA is aligned to the polarization direction x_3. The mechanical and electrical boundary conditions are applied as shown in Fig. 4(a), with a non-zero voltage ϕ.

Under these assumptions, all stress components are equal to zero in the PSA. Furthermore the transverse electric field E_1 is zero, since there are no voltage differences nor charges applied to the surfaces parallel to the x_1 direction. Thus, from the first equation of Eq. (9), we obtain $S_{33} = d_{33} E_3$. As in the 1D model, the electric field in the x_3 direction within a piezoelectric disc is constant and equal to $E_3 = -\frac{\phi}{t_{\text{d}}}$. With $L = n\,t_{\text{d}}$, we obtain

$$\begin{aligned} S_{11} &= -n\,d_{31}\frac{\phi}{L} \\ S_{33} &= -n\,d_{33}\frac{\phi}{L} \end{aligned} \tag{10}$$

The capacitance of the PSA for the 2D case can be obtained similarly to the 1D case, since $E_1 = 0$, yielding the same result as Eq. (4). Therefore, the equivalent properties of a PSA of n discs illustrated in Fig. 4(b) in the strain-charge form are $d_{31_{\text{PSA}}} = n\,d_{31}$,

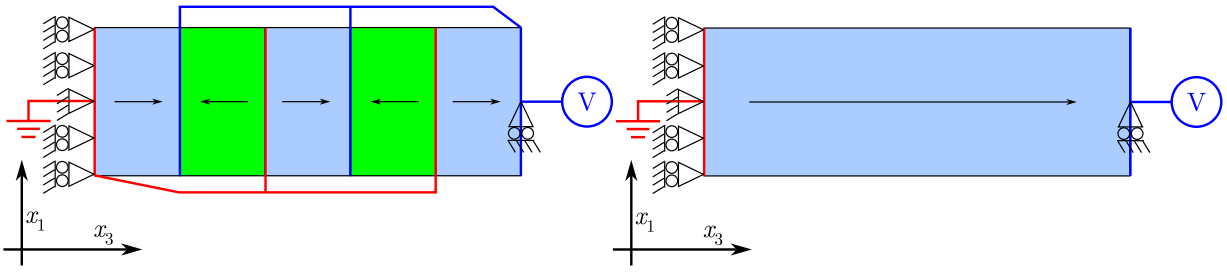

(a) Full model. (b) Equivalent model.

Fig. 4. 2D model of the PSA.

$d_{33_{\text{PSA}}} = n\, d_{33}$ and $\varepsilon^{\text{T}}_{33_{\text{PSA}}} = n^2 \varepsilon^{\text{T}}_{33}$. After using Eq. (7), the following equivalent PSA properties are obtained in the stress-charge form:

$$\begin{aligned} e_{31_{\text{PSA}}} &= n\, e_{31} \\ e_{33_{\text{PSA}}} &= n\, e_{33} \\ \varepsilon^{\text{S}}_{33_{\text{PSA}}} &= n^2 \varepsilon^{\text{S}}_{33} \end{aligned} \tag{11}$$

The three-dimensional (3D) case is a trivial extension of the 2D case, with the equivalent PSA properties in the stress-charge form being the same as the 2D case with an additional $e_{32_{\text{PSA}}} = n\, e_{32}$.

The proposed equivalent PSA model assumes piezoelectric materials of crystalline structure class 4*mm* and has two main limitations. The first one is the assumption of perfect bonding between the piezoelectric discs within the PSA, since in reality the discs are glued together with a bonding material. The other limitation is that the equivalent properties are only valid for the simplified boundary conditions shown in Fig. 4(a), since the PSA may only be connected to a structural material through its ends. In Section 2.3.4 an approach to mitigate the second limitation is presented.

To simplify notation, in the following sections the properties of the equivalent piezoelectric material associated to the qth PSA are referred to as $\boldsymbol{c}^{\text{E}}_q$, $\boldsymbol{e}_q$ and $\boldsymbol{\varepsilon}^{\text{S}}_q$.

2.2. Finite element discretization

The smart structure is designed using density-based TO techniques. The design domain of the structure is represented as Ω and is illustrated in Fig. 1(a). In this work it is discretized with a homogeneous mesh, although the proposed methodology can be straightforwardly adapted to inhomogeneous meshes. The linear constitutive piezoelectric relations shown in Eq. (6) are considered, as well as small deformations and rotations, which are valid assumptions for the analysis of low-voltage actuators [1]. Furthermore, for simplification purposes, 2D plane-strain hypothesis is considered.

Considering small strain relations and that the electric field is equal to minus the gradient of the electric potential, using the variational principle for piezoelectric media and only static excitations, the following equilibrium equation is obtained [50]:

$$\boldsymbol{K}\,\boldsymbol{U} = \begin{bmatrix} \boldsymbol{K}_{\text{uu}} & \boldsymbol{K}^{\top}_{\phi\text{u}} \\ \boldsymbol{K}_{\phi\text{u}} & -\boldsymbol{K}_{\phi\phi} \end{bmatrix} \begin{Bmatrix} \boldsymbol{u} \\ \boldsymbol{\phi} \end{Bmatrix} = \begin{Bmatrix} \boldsymbol{f} \\ \boldsymbol{q} \end{Bmatrix} = \boldsymbol{F} \tag{12}$$

The vectors $\boldsymbol{u}$, $\boldsymbol{\phi}$, $\boldsymbol{f}$ and $\boldsymbol{q}$ are the nodal mechanical displacements, electric potentials, applied forces and electric charges, respectively. The first two are succinctly referred to by the vector $\boldsymbol{U}$ and the last two by $\boldsymbol{F}$. The global stiffness matrix $\boldsymbol{K}$ contains three distinct submatrices, namely the assembled mechanical stiffness $\boldsymbol{K}_{\text{uu}}$, piezoelectric coupling $\boldsymbol{K}_{\phi\text{u}}$ and dielectric $\boldsymbol{K}_{\phi\phi}$ matrices [37,51,52].

In this work, the smart structure is excited by input voltages at the boundaries of the domain $\partial\Omega$. Thus, $\boldsymbol{F} = 0$ and a prescribed non-zero voltage ϕ^* is applied to Eq. (12) together with fixed displacements ($\boldsymbol{u} = 0$) and grounded surfaces ($\boldsymbol{\phi} = 0$). With n_{p} being the number of prescribed degrees of freedom, and an under-tilde representing the subblock of a matrix or a vector corresponding to the free degrees of freedom, the equilibrium equation of the free degrees of freedom can be written as

$$\underset{\sim}{\underset{\sim}{\boldsymbol{K}}}\,\underset{\sim}{\boldsymbol{U}} = -\sum_{j}^{n_{\text{p}}} \underbrace{\begin{bmatrix} \boldsymbol{K}_{\phi\text{u}} \\ -\boldsymbol{K}_{\phi\phi} \end{bmatrix}}_{j} \phi^* \tag{13}$$

The element matrices of element i prior to the assembly procedure are calculated using Gaussian quadrature as

$$\begin{aligned}\boldsymbol{K}_{\mathrm{uu}_i} &= \int_{\Omega_i} \boldsymbol{B}_{\mathrm{u}}^{\top} c^{\mathrm{E}} \boldsymbol{B}_{\mathrm{u}} \,\mathrm{d}\,\Omega \\ \boldsymbol{K}_{\phi\mathrm{u}_i} &= \int_{\Omega_i} \boldsymbol{B}_{\phi}^{\top} \boldsymbol{e}\, \boldsymbol{B}_{\mathrm{u}} \,\mathrm{d}\,\Omega \\ \boldsymbol{K}_{\phi\phi_i} &= \int_{\Omega_i} \boldsymbol{B}_{\phi}^{\top} \boldsymbol{\varepsilon}^{\mathrm{S}} \boldsymbol{B}_{\phi} \,\mathrm{d}\,\Omega\end{aligned} \tag{14}$$

where matrix $\boldsymbol{B}_{\mathrm{u}}$ relates the nodal displacements $\boldsymbol{u}$ with the strain $\boldsymbol{S}$ and $\boldsymbol{B}_{\phi}$ relates the nodal electric potentials $\boldsymbol{\phi}$ with the electric field $\boldsymbol{E}$.

Note that every element in the mesh is modelled as a piezoelectric material. The non-piezoelectric materials are modelled as having zero piezoelectric properties $e_{ij} = 0$ and the conductive material as having a very large isotropic dielectric permittivity value $\varepsilon^{\mathrm{S}}_{ij}$, such that the electric field within it tends to zero when only one voltage value is prescribed [46]. The actual material property that an element may have is determined by interpolating the possible material properties with certain pseudo-densities. The pseudo-densities associated to the actuators are obtained using a geometry projection method, which is introduced in Section 2.3, while the pseudo-densities associated to the material domain are discussed in Section 3.1. Section 3.2 clarifies how the final properties of each element are obtained.

Since the right-hand side of Eq. (13) depends on the global assembled matrix $\boldsymbol{K}$, sensitivity information obtained by differentiating the equilibrium equations with respect to the pseudo-densities used in the TO procedure may be derived directly from Eq. (12), with $\boldsymbol{u}$ containing zeros where the nodal displacements are fixed, $\boldsymbol{\phi}$ containing zeros where the voltages are grounded and ϕ^* where the voltage is prescribed.

It is known that the large differences in orders of magnitude of the mechanical and permittivity properties cause numerical issues due to ill-conditioning of the global stiffness matrix $\boldsymbol{K}$. To mitigate this, the properties are scaled similarly to Homayouni-Amlashi et al. [37].

2.3. PSA geometry modelling

In this work a geometry projection method is applied to model the geometric domain shown in Fig. 1(b). Geometric variables, represented succinctly as $\boldsymbol{x}$, describing the position, size and orientation of rectangular primitives that are used to model the PSA are applied to a signed-distance function $\varphi(\boldsymbol{x}, \boldsymbol{p})$, which can be evaluated at any point in space $\boldsymbol{p}$. This function is in turn passed to a smooth approximate piecewise Heaviside function $\tilde{H}$ that generates a continuous representation of the primitive. In order to obtain element-wise pseudo-densities of the primitive in a fixed grid, $\tilde{H}(\varphi(\boldsymbol{x}, \boldsymbol{p}))$ is evaluated at multiple points $\boldsymbol{p}_j$ within each grid element and a volumetric average is calculated using a second order Newton–Cotes rule. [42]

Each PSA is modelled by stacking three different rectangular geometric primitives on top of each other, for void, electrode and equivalent piezoelectric materials, thus referred to as a "composite projection" scheme, as described in detail in Section 2.3.4. Each pseudo-density is associated to a certain material property. Furthermore, each PSA has an additional "opacity variable" $\alpha \in [0, 1]$ (also called a "size variable" [53] or a "membership variable" [54]), which scales the properties between 0 and 1, so that a PSA may be removed in the optimization process as $\alpha \to 0$.

2.3.1. Rectangular signed-distance function

In the geometry projection method, geometric primitives that may only change in size, position and orientation are described by geometric variables $\boldsymbol{x}$. In this work the geometric primitive is rectangular, in agreement with typical 2D PSA shapes. As shown in Fig. 5, it is described implicitly by a rectangular signed-distance function, with the geometric variables being the coordinates of their extremities $\boldsymbol{x}_0$ and $\boldsymbol{x}_{\mathrm{f}}$ and their width d.

A rectangular signed-distance function $\varphi(\boldsymbol{x}_0, \boldsymbol{x}_{\mathrm{f}}, d, \boldsymbol{p}) = \varphi(\boldsymbol{x}, \boldsymbol{p})$ evaluated at any point in space $\boldsymbol{p}$ that has the boundaries of the rectangular primitive shown in Fig. 5 as its zero-contour line is defined in Eq. (15), with the auxiliary terms defined in Eqs. (16)–(17).

$$\varphi(\boldsymbol{x}, \boldsymbol{p}) = \begin{cases} -\dfrac{\boldsymbol{b}\cdot\boldsymbol{a}}{\|\boldsymbol{a}\|}, & \text{if } \|\boldsymbol{g}\| \le \frac{d}{2} \text{ and } \boldsymbol{b}'\cdot\boldsymbol{a} < -\frac{\sqrt{2}}{2}\|\boldsymbol{b}'\|\|\boldsymbol{a}\| \\ \dfrac{\boldsymbol{e}\cdot\boldsymbol{a}}{\|\boldsymbol{a}\|}, & \text{if } \|\boldsymbol{g}\| \le \frac{d}{2} \text{ and } \boldsymbol{e}'\cdot\boldsymbol{a} > \frac{\sqrt{2}}{2}\|\boldsymbol{e}'\|\|\boldsymbol{a}\| \\ \|\boldsymbol{b}''\|, & \text{if } \|\boldsymbol{g}\| > \frac{d}{2} \text{ and } \boldsymbol{b}\cdot\boldsymbol{a} < 0 \\ \|\boldsymbol{e}''\|, & \text{if } \|\boldsymbol{g}\| > \frac{d}{2} \text{ and } \boldsymbol{e}\cdot\boldsymbol{a} > 0 \\ \|\boldsymbol{g}\| - \dfrac{d}{2}, & \text{otherwise} \end{cases} \tag{15}$$

$$\boldsymbol{a} = \boldsymbol{x}_{\mathrm{f}} - \boldsymbol{x}_0 \qquad \boldsymbol{b} = \boldsymbol{p} - \boldsymbol{x}_0 \qquad \boldsymbol{e} = \boldsymbol{p} - \boldsymbol{x}_{\mathrm{f}} \qquad \boldsymbol{h} = \frac{\boldsymbol{b}\cdot\boldsymbol{a}}{\boldsymbol{a}\cdot\boldsymbol{a}}\boldsymbol{a} \qquad \boldsymbol{g} = \boldsymbol{b} - \boldsymbol{h} \tag{16}$$

$$\boldsymbol{b}' = \boldsymbol{b} - \frac{d}{2}\frac{\boldsymbol{a}}{\|\boldsymbol{a}\|} \qquad \boldsymbol{e}' = \boldsymbol{e} + \frac{d}{2}\frac{\boldsymbol{a}}{\|\boldsymbol{a}\|} \qquad \boldsymbol{b}'' = \boldsymbol{b} - \frac{d}{2}\frac{\boldsymbol{g}}{\|\boldsymbol{g}\|} \qquad \boldsymbol{e}'' = \boldsymbol{e} - \frac{d}{2}\frac{\boldsymbol{g}}{\|\boldsymbol{g}\|} \tag{17}$$

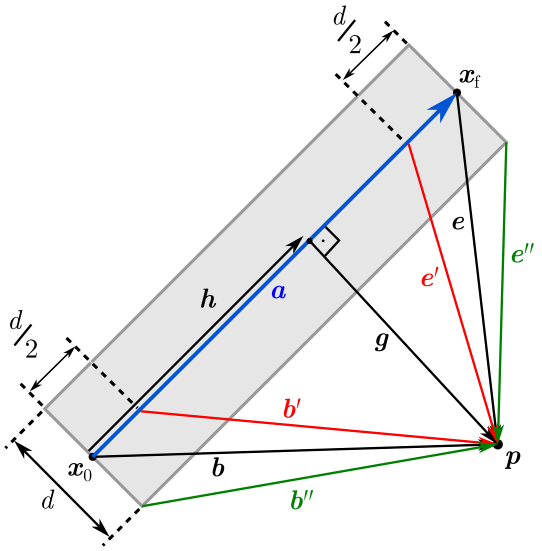

Fig. 5. Rectangular geometric primitive. This figure shows the geometric variables $\boldsymbol{x}_0$, $\boldsymbol{x}_f$ and d, as well as the auxiliary variables utilized to describe a rectangular signed-distance function $\varphi(\boldsymbol{x}, \boldsymbol{p})$ at a point in space $\boldsymbol{p}$.

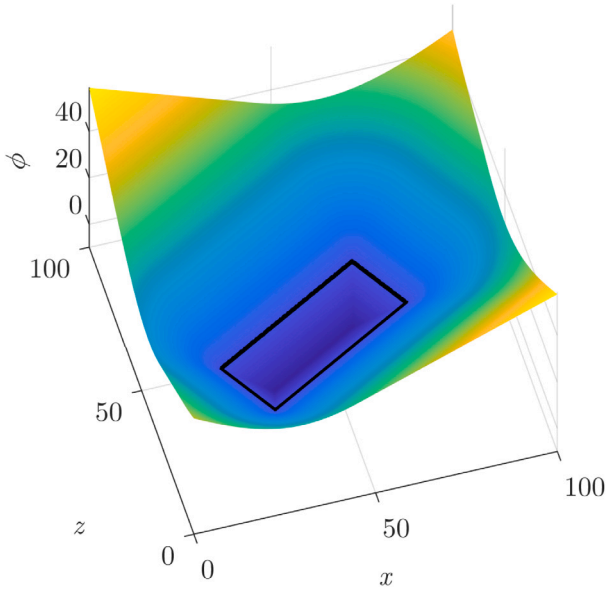

Fig. 6. Surface plot of the rectangular signed-distance function with a mesh with $h = 0.2$ in a 100×100 domain.

Fig. 6 shows a surface plot of the signed-distance function. Outside the boundaries of the rectangle (i.e. the zero-contour line shown in black) it is a C^1 continuous function. Within it and including the line, it is C^0 continuous. The isocontours of the proposed function exactly describe a rectangle, while having the desirable property of signed-distance functions, i.e. that the spatial gradient is unit $\nabla\varphi(\boldsymbol{x}, \boldsymbol{p}) = 1$, which avoids issues that occur when there is a non-equidistant distribution of level-set contours of geometric features [55].

2.3.2. Smooth heaviside function

To classify if points are part of a PSA, the signed-distance function $\varphi(\boldsymbol{x}, \boldsymbol{p})$ defined in the preceding subsection is passed to a smooth approximation of a Heaviside function $\tilde{H}(x)$ shown in Eq. (18). It is a continuous piecewise function with a cubic polynomial interpolation in its transition zone of width w [42]. The output is a continuous scalar field between 0 and 1 that determines whether

a region is outside or within the geometric primitive, respectively.

$$\tilde{H}(x) = \begin{cases} 1, & \text{if } x < -\frac{w}{2} \\ 2\frac{x^3}{w^3} - \frac{3x}{2w} + \frac{1}{2}, & \text{if } |x| \leq \frac{w}{2} \\ 0, & \text{if } x > \frac{w}{2} \end{cases} \tag{18}$$

Smaller values of w make the approximate Heaviside function become sharper, while larger values make it smoother. A value of $w = 2h$ is chosen in this work, where h is the mesh size and is shown in Fig. 7(a). For illustration purposes, the plot obtained for a larger transition zone of $w = 20h$ is shown in Fig. 7(b).

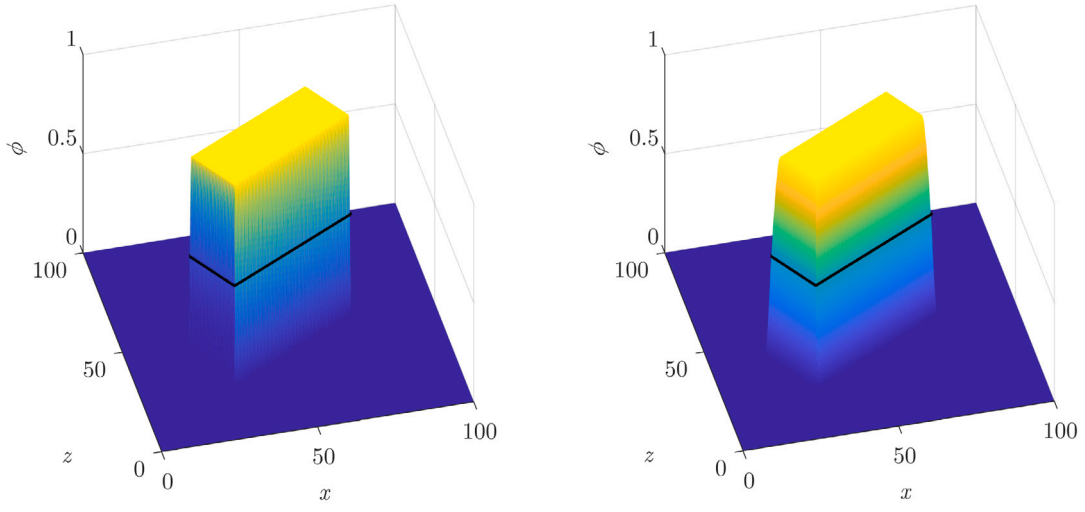

(a) $w = 2h$ (b) $w = 20h$

Fig. 7. Plots of $\tilde{H}(\boldsymbol{x})$ with $h = 0.2$ in a 100×100 domain, for the signed-distance function shown in Fig. 6 with different transition zone widths w.

2.3.3. Projection into a fixed grid

The scalar field $\tilde{H}(\varphi(\boldsymbol{x}, \boldsymbol{p})) \in [0, 1]$ has to be processed in order for each element to have a unique constant pseudo-density associated to it. This can be done by performing a volume averaging of $\tilde{H}(\varphi(\boldsymbol{x}, \boldsymbol{p}))$ within each element, which can be written mathematically as:

$$\rho_i(\boldsymbol{x}) = \frac{1}{V_i} \int_{\Omega_i} \tilde{H}(\varphi(\boldsymbol{x}, \boldsymbol{p}))\, \mathrm{d}\,\Omega \tag{19}$$

where Ω_i is the volume of element i and $V_i = |\Omega_i|$.

In this work, the closed second-order Newton–Cotes rule [42] (i.e. Simpson's one-third rule) is used to calculate the above integration numerically. Writing the weights of this integration rule as w_j for N integration points and $j = 1, \ldots, N$, then ρ_i can be expressed as:

$$\rho_i(\boldsymbol{x}) = \sum_{j}^{N} w_j \tilde{H}_{ij} \tag{20}$$

where $\tilde{H}_{ij}$ is obtained by calculating $\tilde{H}(\varphi(\boldsymbol{x}, \boldsymbol{p}_j))$ at a point in space $\boldsymbol{p}_j$ within element i. For 2D quadrilateral elements, $N = 3^2 = 9$.

2.3.4. Composite projection

To mitigate the second limitation of the equivalent PSA material model mentioned at the end of Section 2.1, thin orthotropic conductive layers are attached to the ends of the PSA, which are stiff only in the direction aligned to the PSA, and compliant in the other directions, shown as the red region in Fig. 8. For example, c^{E}_{33} may be equal to that of steel, but c^{E}_{11}, c^{E}_{13} and c^{E}_{55} are significantly smaller. Additionally, an enveloping void region is added to the sides of the PSA to exclusively permit connections between the equivalent piezoelectric material and the surrounding structure of the mechanism where it is embedded in at the ends of the PSA.

Each material region of the PSA shown in Fig. 8 can be described by a distinct geometric primitive using the geometry projection method. So to obtain a density-based representation of the PSA in a fixed mesh, three different pseudo-density fields are obtained following the methodology shown in the preceding subsections, associated to a void region $\boldsymbol{\rho}_{\mathrm{v}}$, an electrode region $\boldsymbol{\rho}_{\mathrm{e}}$ and a piezoelectric region $\boldsymbol{\rho}_{\mathrm{p}}$, respectively.

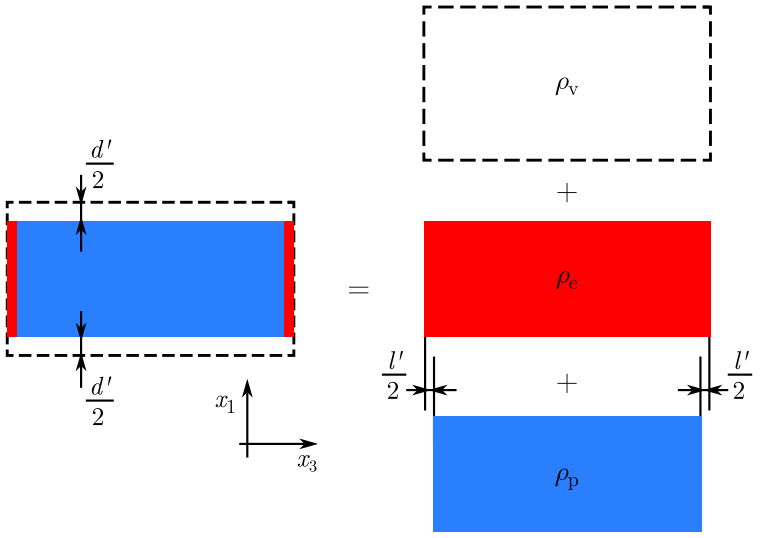

Fig. 8. Composite PSA model using geometry projection. (For interpretation of the references to colour in this figure legend, the reader is referred to the web version of this article.)

From Fig. 8, the pseudo-densities of the piezoelectric region in the composite PSA representation shown in blue are ρ_p. These densities are obtained by considering the geometric parameters $\boldsymbol{x}_0$, $\boldsymbol{x}_f$ and d without any modifications and can be written as a function of $\rho(\boldsymbol{x})$ from Eq. (20).

$$\rho_p = \rho(\boldsymbol{x}_0, \boldsymbol{x}_f, d) \tag{21}$$

The pseudo-densities of the electrode region ρ_e, shown in red, are obtained considering a length-wise offset of the blue region by a fixed value l'. Finally the densities ρ_v of the void region, shown in white with dashed lines on the boundary, are obtained by an additional fixed offset of the diameter d'.

We write new offset ("os") geometric design variables $\boldsymbol{x}_0^{os}$, $\boldsymbol{x}_f^{os}$ and d^{os} as

$$\begin{aligned} \boldsymbol{x}_0^{os} &= \boldsymbol{x}_0 - \frac{l'}{2}\frac{\boldsymbol{a}}{\|\boldsymbol{a}\|} \\ \boldsymbol{x}_f^{os} &= \boldsymbol{x}_f + \frac{l'}{2}\frac{\boldsymbol{a}}{\|\boldsymbol{a}\|} \\ d^{os} &= d + d' \end{aligned} \tag{22}$$

where $\boldsymbol{a}$ was defined in Eq. (16) and is a vector that goes from the initial extremity of the PSA defined by coordinate $\boldsymbol{x}_0$ to the other extremity defined by $\boldsymbol{x}_f$. Its norm $\|\boldsymbol{a}\|$ is equal to the length L of the piezoelectric region of the PSA, which determines the number of piezoelectric discs n for a given fixed disc thickness t_d used for the calculation of the equivalent piezoelectric material properties shown prior in Section 2.1.

With these, ρ_e and ρ_v are defined as

$$\rho_e = \rho\left(\boldsymbol{x}_0^{os}, \boldsymbol{x}_f^{os}, d\right) \tag{23}$$

$$\rho_v = \rho\left(\boldsymbol{x}_0^{os}, \boldsymbol{x}_f^{os}, d^{os}\right) \tag{24}$$

Note that, from an implementation point of view, since the rectangular signed-distance function is only exactly rectangular at its zero contour line, and assuming for simplicity that $d' = l'$, it is not possible to define ρ_v by first calculating $\varphi(\boldsymbol{x}_0, \boldsymbol{x}_f, d, \boldsymbol{p})$ for ρ_p and then taking a contour line at a different level (e.g. $\varphi(\boldsymbol{x}_0, \boldsymbol{x}_f, d) - d'$) to determine ρ_v, as can be done for the bar-like geometric primitives with rounded edges from Norato et al. [43] or from Wang et al. [56].

2.3.5. PSA finite element matrices

In Section 2.2, the equilibrium equation Eq. (12) was derived from the constitutive equations Eq. (6) without specifying in which coordinate system the properties were defined. As mentioned in Section 2.1, by convention the polarization direction of a piezoelectric material is the x_3 direction [49]. However the material properties of the piezoelectric material in the PSAs are defined such that their local x_3 axis is aligned to their actuation directions, i.e. vector $\boldsymbol{a}$ from Eq. (16). Thus, the properties of the piezoelectric material of each actuator must be rotated to the global coordinate system before being assembled.

Henceforth an apostrophe ($'$) will indicate the local coordinate system of each PSA and the elasticity $\boldsymbol{c}_q^{\mathrm{E}}$, piezoelectric coupling $\boldsymbol{e}_q$ and permittivity $\boldsymbol{\varepsilon}_q^{\mathrm{S}}$ matrices in the global coordinate system of the qth actuator are calculated as

$$\begin{aligned}\boldsymbol{c}_q^{\mathrm{E}} &= \boldsymbol{T}_{\mathrm{a}_q}^{\top}\boldsymbol{c}_q^{\mathrm{E}\prime}\boldsymbol{T}_{\mathrm{a}_q}\\ \boldsymbol{e}_q &= \boldsymbol{R}_{\mathrm{a}_q}^{\top}\boldsymbol{e}_q'\boldsymbol{T}_{\mathrm{a}_q}\\ \boldsymbol{\varepsilon}_q^{\mathrm{S}} &= \boldsymbol{R}_{\mathrm{a}_q}^{\top}\boldsymbol{\varepsilon}_q^{\mathrm{S}\prime}\boldsymbol{R}_{\mathrm{a}_q}\end{aligned} \tag{25}$$

From Cook et al. [57, Ch. 2], and utilizing the vector $\boldsymbol{a}_q$, which in 2D has components a_{q_x} and a_{q_z}, the tensor $\boldsymbol{T}_{\mathrm{a}_q}$ and vector $\boldsymbol{R}_{\mathrm{a}_q}$ rotation matrices in a 2D setting are defined respectively as:

$$\boldsymbol{R}_{\mathrm{a}_q} = \frac{1}{\|\boldsymbol{a}_q\|}\begin{bmatrix} a_{q_z} & -a_{q_x} \\ a_{q_x} & a_{q_z}\end{bmatrix} \tag{26}$$

$$\boldsymbol{T}_{\mathrm{a}_q} = \frac{1}{\|\boldsymbol{a}_q\|^2}\begin{bmatrix} a_{q_z}^2 & a_{q_x}^2 & -a_{q_x}a_{q_z} \\ a_{q_x}^2 & a_{q_z}^2 & a_{q_x}a_{q_z} \\ 2a_{q_x}a_{q_z} & -2a_{q_x}a_{q_z} & a_{q_z}^2 - a_{q_x}^2\end{bmatrix} \tag{27}$$

In a 3D setting, the signed-distance function given in Eq. (15) represents a cylinder. Since we only consider transversely isotropic piezoelectric materials, some simplifications can be made to the corresponding 3D tensor and vector rotation matrices [57, Ch. 2], which is left for future works.

Therefore, the element-level matrices of element i related to actuator q can be written by inserting the rotated property matrices of Eq. (25) into Eq. (14). This is performed for all submatrices, namely the mechanical $\boldsymbol{K}_{\mathrm{uu}}$, piezoelectric $\boldsymbol{K}_{\phi\mathrm{u}}$ and dielectric $\boldsymbol{K}_{\phi\phi}$ submatrices, for both the electrode material and the equivalent piezoelectric material of each PSA, which are succinctly denoted as $\boldsymbol{K}_{\mathrm{E}_{iq}}$ and $\boldsymbol{K}_{\mathrm{P}_{iq}}$, respectively.

With the element matrices of the electrode and piezoelectric regions defined, together with the element matrices of the void material $\boldsymbol{K}_{\mathrm{V}_i}$, which are calculated as shown in Eq. (14) with the properties attributed to void materials, and with the pseudo-densities shown in the previous subsection, the finite element submatrices of the ith element related to the qth actuator $\boldsymbol{K}_{\mathrm{A}_{iq}}$ are given by Eq. (28), where $\alpha_q \in [0,1]$ is the aforementioned "opacity variable" that allows the optimization process to remove a PSA.

$$\begin{aligned}\boldsymbol{K}_{\mathrm{A}_{\mathrm{uu}_{iq}}} &= \rho_{\mathrm{v}_{iq}}^{w_{\mathrm{a}_{\mathrm{uu}}}}\boldsymbol{K}_{\mathrm{V}_{\mathrm{uu}_i}} + \left(\alpha_q\rho_{\mathrm{e}_{iq}}\right)^{w_{\mathrm{a}_{\mathrm{uu}}}}\left(\boldsymbol{K}_{\mathrm{E}_{\mathrm{uu}_{iq}}} - \boldsymbol{K}_{\mathrm{V}_{\mathrm{uu}_i}}\right) + \left(\alpha_q\rho_{\mathrm{p}_{iq}}\right)^{w_{\mathrm{a}_{\mathrm{uu}}}}\left(\boldsymbol{K}_{\mathrm{P}_{\mathrm{uu}_{iq}}} - \boldsymbol{K}_{\mathrm{E}_{\mathrm{uu}_{iq}}}\right)\\ \boldsymbol{K}_{\mathrm{A}_{\phi\mathrm{u}_{iq}}} &= \rho_{\mathrm{v}_{iq}}^{w_{\mathrm{a}_{\phi\mathrm{u}}}}\boldsymbol{K}_{\mathrm{V}_{\phi\mathrm{u}_i}} + \left(\alpha_q\rho_{\mathrm{e}_{iq}}\right)^{w_{\mathrm{a}_{\phi\mathrm{u}}}}\left(\boldsymbol{K}_{\mathrm{E}_{\phi\mathrm{u}_{iq}}} - \boldsymbol{K}_{\mathrm{V}_{\phi\mathrm{u}_i}}\right) + \left(\alpha_q\rho_{\mathrm{p}_{iq}}\right)^{w_{\mathrm{a}_{\phi\mathrm{u}}}}\left(\boldsymbol{K}_{\mathrm{P}_{\phi\mathrm{u}_{iq}}} - \boldsymbol{K}_{\mathrm{E}_{\phi\mathrm{u}_{iq}}}\right)\\ \boldsymbol{K}_{\mathrm{A}_{\phi\phi_{iq}}} &= \rho_{\mathrm{v}_{iq}}^{w_{\mathrm{a}_{\phi\phi}}}\boldsymbol{K}_{\mathrm{V}_{\phi\phi_i}} + \left(\alpha_q\rho_{\mathrm{e}_{iq}}\right)^{w_{\mathrm{a}_{\phi\phi}}}\left(\boldsymbol{K}_{\mathrm{E}_{\phi\phi_{iq}}} - \boldsymbol{K}_{\mathrm{V}_{\phi\phi_i}}\right) + \left(\alpha_q\rho_{\mathrm{p}_{iq}}\right)^{w_{\mathrm{a}_{\phi\phi}}}\left(\boldsymbol{K}_{\mathrm{P}_{\phi\phi_{iq}}} - \boldsymbol{K}_{\mathrm{E}_{\phi\phi_{iq}}}\right)\end{aligned} \tag{28}$$

The penalization values $\boldsymbol{w}_{\mathrm{a}} = [w_{\mathrm{a}_{\mathrm{uu}}}, w_{\mathrm{a}_{\phi\mathrm{u}}}, w_{\mathrm{a}_{\phi\phi}}]$ are SIMP interpolation exponents. The specific values used in the manuscript are given in Section 5. Section 3.2 shows how each single finite element submatrix is obtained by combining all individual submatrices of $\boldsymbol{K}_{\mathrm{A}_{iq}}$ associated to each actuator.

Note that in Eq. (28) the α_q variable does not multiply the pseudo-density ρ_{v} associated to the void region of the PSA, which means that as $\alpha_q \to 0$, the PSA becomes a rectangular void region. If instead α_q also multiplied ρ_{v}, then the void region enveloping the piezoelectric material of the PSA would become transparent for intermediate α_q values, allowing the sides of the PSA to electrically connect to the surrounding conductive material of the material domain. Due to the width d of the PSA being smaller than its length, the transverse electric field component E_1' would be larger than its lengthwise component E_3'. Extra non-physical piezoelectric actuation could be attained by benefiting from the piezoelectric shear-mode e_{15}', which would yield non-physical designs in the optimization process.

3. Material interpolation

While the previous section dealt with the description of the geometric set, this section is concerned with the material set, illustrated in Fig. 1(c). The whole domain Ω is divided into a void region Ω_{V} and a solid region Ω_{S}, which in turn is divided into a dielectric region Ω_{D} and a conductive region Ω_{C}, such that $\Omega = \Omega_{\mathrm{V}} \cup \Omega_{\mathrm{S}} = \Omega_{\mathrm{V}} \cup \Omega_{\mathrm{D}} \cup \Omega_{\mathrm{C}}$ and the last three regions are mutually exclusive. The material properties of each of these domains is derived in Section 3.1 using a three-field SIMP interpolation. Section 3.2 then describes how the element stiffness matrices obtained from the preceding sections are interpolated together yielding a mathematical representation for the properties of the combined domain Ω, illustrated in Fig. 1(a).

3.1. Multimaterial three-phase interpolation

Simultaneously with the position, size and orientation of the PSAs, the design of the structure in which the PSA is embedded is also optimized. This domain is represented as the material set in Fig. 1(c). Density-based TO is applied considering two design variables, which are used to interpolate between void, dielectric and conductive materials. The solid–void densities $\boldsymbol{\rho}_{\mathrm{sv}}$ control whether each element should be void (0) or solid (1), and the conductive–dielectric densities $\boldsymbol{\rho}_{\mathrm{cd}}$ control whether they should be dielectric (0) or conductive (1).

A three-phase SIMP interpolation [8,58,59] is used to interpolate the properties of the material domain. Since only linear hypotheses are considered, the interpolation may be applied directly to the ith element stiffness matrices. The submatrices of the solid domain of the ith element $\boldsymbol{K}_{\mathrm{S}_i}$ may be written as:

$$\begin{aligned}
\boldsymbol{K}_{\mathrm{S}_{\mathrm{uu}_i}} &= \hat{\tilde{\rho}}_{\mathrm{cd}_i}^{w_{\mathrm{cd}_{\mathrm{uu}}}} \boldsymbol{K}_{\mathrm{C}_{\mathrm{uu}_i}} - \left(1 - \hat{\tilde{\rho}}_{\mathrm{cd}_i}\right)^{w_{\mathrm{cd}_{\mathrm{uu}}}} \boldsymbol{K}_{\mathrm{D}_{\mathrm{uu}_i}} \\
\boldsymbol{K}_{\mathrm{S}_{\phi\mathrm{u}_i}} &= \hat{\tilde{\rho}}_{\mathrm{cd}_i}^{w_{\mathrm{cd}_{\phi\mathrm{u}}}} \boldsymbol{K}_{\mathrm{C}_{\phi\mathrm{u}_i}} - \left(1 - \hat{\tilde{\rho}}_{\mathrm{cd}_i}\right)^{w_{\mathrm{cd}_{\phi\mathrm{u}}}} \boldsymbol{K}_{\mathrm{D}_{\phi\mathrm{u}_i}} \\
\boldsymbol{K}_{\mathrm{S}_{\phi\phi_i}} &= \hat{\tilde{\rho}}_{\mathrm{cd}_i}^{w_{\mathrm{cd}_{\phi\phi}}} \boldsymbol{K}_{\mathrm{C}_{\phi\phi_i}} - \left(1 - \hat{\tilde{\rho}}_{\mathrm{cd}_i}\right)^{w_{\mathrm{cd}_{\phi\phi}}} \boldsymbol{K}_{\mathrm{D}_{\phi\phi_i}}
\end{aligned} \tag{29}$$

where the subscripts "C" and "D" mean "conductive" and "dielectric", respectively. The SIMP exponents $\boldsymbol{w}_{\mathrm{cd}} = [w_{\mathrm{cd}_{\mathrm{uu}}}, w_{\mathrm{cd}_{\phi\mathrm{u}}}, w_{\mathrm{cd}_{\phi\phi}}]$ are only used for interpolating between the conductive and dielectric matrices and their values are given in Section 5. The tilde ($\sim$) denotes fields produced by the standard convolutional or density filter and the hat ($\wedge$) accent symbolizes the following smooth Heaviside projection

$$\hat{x}(x) = H(x) = \frac{\tanh\beta\eta + \tanh\beta(x-\eta)}{\tanh\beta\eta + \tanh\beta(1-\eta)} \tag{30}$$

where β is a sharpness parameter and η is a threshold parameter. In this work $\eta = 0.5$. The value of β is initially a small value and increases during the design process using a continuation approach as defined in Section 4.

The submatrices of the material domain of the ith element $\boldsymbol{K}_{\mathrm{M}_i}$ can be subsequently written as:

$$\begin{aligned}
\boldsymbol{K}_{\mathrm{M}_{\mathrm{uu}_i}} &= \hat{\tilde{\rho}}_{\mathrm{sv}_i}^{w_{\mathrm{sv}_{\mathrm{uu}}}} \boldsymbol{K}_{\mathrm{S}_{\mathrm{uu}_i}} + \left(1 - \hat{\tilde{\rho}}_{\mathrm{sv}_i}^{w_{\mathrm{sv}_{\mathrm{uu}}}}\right) \boldsymbol{K}_{\mathrm{V}_{\mathrm{uu}_i}} \\
\boldsymbol{K}_{\mathrm{M}_{\phi\mathrm{u}_i}} &= \hat{\tilde{\rho}}_{\mathrm{sv}_i}^{w_{\mathrm{sv}_{\phi\mathrm{u}}}} \boldsymbol{K}_{\mathrm{S}_{\phi\mathrm{u}_i}} + \left(1 - \hat{\tilde{\rho}}_{\mathrm{sv}_i}^{w_{\mathrm{sv}_{\phi\mathrm{u}}}}\right) \boldsymbol{K}_{\mathrm{V}_{\phi\mathrm{u}_i}} \\
\boldsymbol{K}_{\mathrm{M}_{\phi\phi_i}} &= \hat{\tilde{\rho}}_{\mathrm{sv}_i}^{w_{\mathrm{sv}_{\phi\phi}}} \boldsymbol{K}_{\mathrm{S}_{\phi\phi_i}} + \left(1 - \hat{\tilde{\rho}}_{\mathrm{sv}_i}^{w_{\mathrm{sv}_{\phi\phi}}}\right) \boldsymbol{K}_{\mathrm{V}_{\phi\phi_i}}
\end{aligned} \tag{31}$$

where the SIMP exponents $\boldsymbol{w}_{\mathrm{sv}} = [w_{\mathrm{sv}_{\mathrm{uu}}}, w_{\mathrm{sv}_{\phi\mathrm{u}}}, w_{\mathrm{sv}_{\phi\phi}}]$ are only used for interpolating between the solid and void submatrices, and their values are given in Section 5.

In this work, void material has a very small Young's modulus and the permittivity of air. Dielectric material also has the permittivity of air. Conductive material has a very large permittivity value. Because of the large difference in orders of magnitude between the permittivities of void and conductive materials, the stiffness matrix $\tilde{\boldsymbol{K}}$ of the equilibrium equation (12) can become ill-conditioned, even with the scaling of the properties. Therefore, diagonal scaling of $\tilde{\boldsymbol{K}}$ is performed prior to solving the linear system [57].

3.2. Full domain interpolation

In this section the formulation of the element matrix that combines both the geometric and the material domains of Fig. 1(a) is presented. Since each PSA has an orthotropic material aligned to its own orientation and its own α_q term, if the stiffness matrices of the PSAs $\boldsymbol{K}_{\mathrm{A}_{iq}}$ were simply added together, this would mean that an element would have properties of more than one PSA, were they to overlap.

Instead, firstly a soft-argument-maximum function, or softargmax, term σ is used to evaluate $\alpha_q \rho_{\mathrm{v}_{iq}}$ for each component at every element, as done in [53], yielding a value close to 1 for the PSA with largest $(\alpha_q \rho_{\mathrm{v}_{iq}})^{\boldsymbol{w}_{\mathrm{a}}}$ and a value close to 0 for all other PSAs. The result of this softargmax for the mechanical and piezoelectric submatrices is calculated as

$$\sigma_{\mathrm{uu}_{iq}} = \frac{e^{\kappa(\alpha_q \rho_{\mathrm{v}_{iq}})^{w_{\mathrm{a}_{\mathrm{uu}}}}}}{\sum_j^{n_{\mathrm{a}}} e^{\kappa(\alpha_j \rho_{\mathrm{v}_{ij}})^{w_{\mathrm{a}_{\mathrm{uu}}}}}} \quad \text{and} \quad \sigma_{\phi\mathrm{u}_{iq}} = \frac{e^{\kappa(\alpha_q \rho_{\mathrm{v}_{iq}})^{w_{\mathrm{a}_{\phi\mathrm{u}}}}}}{\sum_j^{n_{\mathrm{a}}} e^{\kappa(\alpha_j \rho_{\mathrm{v}_{ij}})^{w_{\mathrm{a}_{\phi\mathrm{u}}}}}} \tag{32}$$

where κ is a sharpness parameter equal to 50 in this work, and n_{a} is the total number of actuators.

In order to avoid the issue of the softargmax becoming too small due to the α_q term such that it would make the enveloping void region of the PSA become slightly "transparent", enabling transverse electrical connections between the PSA and the underlying conductive material, the softargmax parameter $\sigma_{\phi\phi_{iq}}$ for the dielectric submatrix is calculated without the α_q term:

$$\sigma_{\phi\phi_{iq}} = \frac{e^{\kappa \rho_{\mathrm{v}_{iq}}^{w_{\mathrm{a}_{\phi\phi}}}}}{\sum_j^{n_{\mathrm{a}}} e^{\kappa \rho_{\mathrm{v}_{ij}}^{w_{\mathrm{a}_{\phi\phi}}}}} \tag{33}$$

Finally, the element submatrices of element i that combine the element submatrices of each of the separate geometric and material sets shown in Figs. 1(b) and 1(c), respectively, can be written as

$$\begin{aligned}
\boldsymbol{K}_{\mathrm{uu}_i} &= \sum_{q}^{n_\mathrm{a}} \sigma_{\mathrm{uu}_{iq}} \boldsymbol{K}_{\mathrm{A}_{\mathrm{uu}_{iq}}} + \left(1 - \sum_{q}^{n_\mathrm{a}} \sigma_{\mathrm{uu}_{iq}} \rho_{\mathrm{v}_{iq}}^{w_{\mathrm{a}_{\mathrm{uu}}}}\right) \boldsymbol{K}_{\mathrm{M}_{\mathrm{uu}_i}} \\
\boldsymbol{K}_{\phi\mathrm{u}_i} &= \sum_{q}^{n_\mathrm{a}} \sigma_{\phi\mathrm{u}_{iq}} \boldsymbol{K}_{\mathrm{A}_{\phi\mathrm{u}_{iq}}} + \left(1 - \sum_{q}^{n_\mathrm{a}} \sigma_{\phi\mathrm{u}_{iq}} \rho_{\mathrm{v}_{iq}}^{w_{\mathrm{a}_{\phi\mathrm{u}}}}\right) \boldsymbol{K}_{\mathrm{M}_{\phi\mathrm{u}_i}} \\
\boldsymbol{K}_{\phi\phi_i} &= \sum_{q}^{n_\mathrm{a}} \sigma_{\phi\phi_{iq}} \boldsymbol{K}_{\mathrm{A}_{\phi\phi_{iq}}} + \left(1 - \sum_{q}^{n_\mathrm{a}} \sigma_{\phi\phi_{iq}} \rho_{\mathrm{v}_{iq}}^{w_{\mathrm{a}_{\phi\phi}}}\right) \boldsymbol{K}_{\mathrm{M}_{\phi\phi_i}}
\end{aligned} \tag{34}$$

In elements where there are no actuators, $\rho_{\mathrm{v}_{iq}} = 0$. This means that the first term in every equation of Eq. (34) is zero and the term within the parentheses is equal to 1. Thus, the properties of these elements are exclusively determined by the material matrix interpolation $\boldsymbol{K}_{\mathrm{M}_i}$ of Eq. (31). Conversely, in elements where there is at least one actuator, σ_{iq} will have a value close to 1 for one of the actuators and a value close to 0 for the others. Then the term in the parentheses will approach 0 and the properties of the element will be predominantly determined by the actuator with the largest σ_{iq} value, $\boldsymbol{K}_{\mathrm{A}_{iq}}$ of Eq. (28).

4. Smart structure design topology optimization formulation

The smart structure is initially described by a general design domain shown in Fig. 9, containing n_a PSAs represented by the variables $\boldsymbol{x}_0$, $\boldsymbol{x}_f$, d and α introduced in Section 2.3 and an initial distribution of void, dielectric and conductive materials, represented via the density-based variables $\boldsymbol{\rho}_{\mathrm{sv}}$ and $\boldsymbol{\rho}_{\mathrm{cd}}$ discussed in Section 3.1.

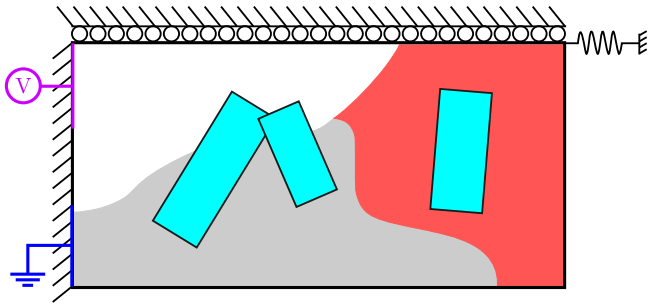

Fig. 9. Design domain and boundary conditions of the smart structure.

Boundary conditions are imposed based on the desired application. For example, in Fig. 9 the design is clamped in the left-hand side, rollers are applied on the upper surface, the lower-left surface is electrically grounded and a non-zero (prescribed) voltage is applied to the upper-left surface. A spring is connected to a degree of freedom where a displacement is to be maximized, representing a workpiece stiffness.

The design of the smart structure is obtained by performing density-based TO, seeking to maximize the displacement of the node connected to the spring. In the following subsection, the formal mathematical statement of the optimization problem is given and the constraints that are applied to obtain feasible designs are introduced and discussed.

Next, the sensitivities of the objective and constraint functions with respect to the design variables are provided, as well as the derivatives of the stiffness matrices from Sections 2.3.5 and 3.1. The derivatives of the equivalent piezoelectric properties from Section 2.1 and of the variables calculated from the geometry projection method in Section 2.3 are given in Appendix A. An overview of the optimization algorithm is presented in Section 4.6.

In the closing subsection details are given on the optimization parameters, such as the parameters used for the Method of Moving Asymptotes (MMA) [60] and how the continuation approach was applied to the Heaviside projection sharpness parameter β.

4.1. Optimization problem and objective function

The negative-null form of the optimization problem is shown in Eq. (35).

$$\begin{aligned}
\underset{\{\boldsymbol{x}_0\},\{\boldsymbol{x}_\mathrm{f}\},\boldsymbol{d},\boldsymbol{\alpha},\boldsymbol{\rho}_{\mathrm{sv}},\boldsymbol{\rho}_{\mathrm{cd}}}{\text{minimize}} \quad & f = \boldsymbol{L}^\top \boldsymbol{u} = \begin{Bmatrix} \boldsymbol{L} \\ \boldsymbol{0} \end{Bmatrix}^\top \boldsymbol{U} \\
\text{subject to} \quad & g_\mathrm{v} \leq 0 \\
& g_\mathrm{no} \leq 0 \\
& g_\mathrm{pol} \leq 0 \\
& L_{\min} \leq \|\boldsymbol{a}_q\| \leq L_{\max} \\
& q = 1, \ldots, n_\mathrm{a}
\end{aligned} \tag{35}$$

In the problem statement Eq. (35), $\{\boldsymbol{x}_0\}$ and $\{\boldsymbol{x}_\mathrm{f}\}$ indicate vectors containing all of the initial and end coordinates of all PSAs, respectively. Further, the widths d_q and opacity terms α_q of all PSAs are stacked together in vectors, $\boldsymbol{d}$ and $\boldsymbol{\alpha}$. Functions g_v, g_no and g_pol are the volume, non-overlap and polarization constraints, respectively, and are introduced in the subsequent subsections.

In the objective function f, $\boldsymbol{L}$ is a vector of 0's with a 1 (or a -1, depending on whether it should minimize or maximize) at the position of the degree of freedom corresponding to the displacement in vector $\boldsymbol{u}$ that should be minimized (or maximized), where $\boldsymbol{u}$ are the nodal mechanical displacements obtained by solving the equilibrium equation (12).

The lengths of the PSAs are constrained using $\boldsymbol{a}$ from Eq. (16). A minimum length L_min is imposed on every PSA to avoid a possible edge case during the optimization process where $\boldsymbol{x}_0$ and $\boldsymbol{x}_\mathrm{f}$ coincide, making $\boldsymbol{a}$ go to $\boldsymbol{0}$ and causing division by zero in the signed-distance function Eq. (15), since $\|\boldsymbol{a}\| = 0$. The optimizer can remove an actuator through its α_q variable instead. The maximum lengths L_max may be based on catalogues of manufacturers, for example.

For the box constraints, $\alpha_q, \rho_{\mathrm{sv}_i}, \rho_{\mathrm{cd}_i} \in [0,1]$, with $q = 1,\dots,n_\mathrm{a}$ and $i = 1,\dots,n_\mathrm{e}$, where n_e is the total number of elements in the mesh. $\boldsymbol{x}_{0_q}$ and $\boldsymbol{x}_{\mathrm{f}_q}$ are constrained to be within the boundaries of the design domain, i.e. $\boldsymbol{x}_{0_q}, \boldsymbol{x}_{\mathrm{f}_q} \in \Omega$. And $d_q \in [d_\mathrm{min}, d_\mathrm{max}]$, $q = 1,\dots,n_\mathrm{a}$, with the minimum and maximum widths taken from catalogues of manufacturers, for example. Also, d_min should be greater than $2h$, with h being the element edge length, to avoid division by zero from vector $\boldsymbol{g}$ in the signed-distance function Eq. (15).

4.2. Volume constraint

In the optimization process the maximum amount of solid material is constrained. It is a limit on the ratio between the volume of solid material where there are no actuators, i.e. the volume of $\Omega_\mathrm{S} \cap \Omega_\mathrm{A}^\mathrm{c}$, and the volume of the total non-actuator region, i.e. $\Omega_\mathrm{A}^\mathrm{c}$. If V_f is the maximum solid volume fraction and V_i is the volume of element i, then the constraint g_v can be written as

$$g_\mathrm{v} = \frac{\sum_i^{n_\mathrm{e}} V_i \hat{\rho}_{\mathrm{sv}_i} \left(1 - \sum_q^{n_\mathrm{a}} \sigma_{\mathrm{v}_{iq}} \alpha_q \rho_{\mathrm{v}_{iq}}\right)}{\sum_i^{n_\mathrm{e}} V_i \left(1 - \sum_q^{n_\mathrm{a}} \sigma_{\mathrm{v}_{iq}} \alpha_q \rho_{\mathrm{v}_{iq}}\right)} - V_\mathrm{f} \tag{36}$$

The softargmax parameter $\sigma_{\mathrm{v}_{iq}}$ is calculated as shown in Eq. (37), where the sharpness parameter κ is the same as in Eqs. (32) and (33).

$$\sigma_{\mathrm{v}_{iq}} = \frac{e^{\kappa \alpha_q \rho_{\mathrm{v}_{iq}}}}{\sum_j^{n_\mathrm{a}} e^{\kappa \alpha_j \rho_{\mathrm{v}_{ij}}}} \tag{37}$$

4.3. Non-overlap constraint

It does not make physical sense for two or more actuators to overlap, so a non-overlap constraint is added to the optimization problem. However, the constraint should be relaxed to allow for the overlap of "transparent" PSAs during the design process. Thus, a non-overlap constraint is formulated similarly to [39,61], but adapted for the pseudo-density based design of the geometry projection method, while taking the α_q values into account.

The idea, as illustrated in Fig. 6 of [39], is that the sum of the volumes of all actuators must be always equal to the sum of the volume of the elements where there are any actuators. This can be changed to an inequality constraint, since the former should never be less than the latter, yielding g_no:

$$g_\mathrm{no} = \sum_i^{n_\mathrm{e}} \sum_q^{n_\mathrm{a}} H_\mathrm{no}(\alpha_q \rho_{\mathrm{e}_{iq}}) V_i - \sum_i^{n_\mathrm{e}} H_\mathrm{no}\left(\sum_q^{n_\mathrm{a}} \alpha_q \rho_{\mathrm{e}_{iq}}\right) V_i - \tau \tag{38}$$

where τ is a tolerance, which facilitates the scaling of the constraint for the MMA and can be equal to half of the volume the smallest element in inhomogeneous meshes, for example. V_i is the volume of element i and H_no is the smooth Heaviside projection Eq. (30) with a different sharpness parameter, $\beta_\mathrm{no} = 10$, and a different threshold $\eta_\mathrm{no} = 0.1$. Note that even if two or more PSAs overlap, if the sum of their α_q values is less than 1, then the overlap constraint is not violated.

4.4. Polarization constraint

In the considered problem setting, the applied electric field is controlled by the optimizer, and in principle PSAs acting in tension could be generated. To prevent this from happening, a polarization constraint is proposed, based on the idea of constraining the piezoelectric contribution to the stress to always be negative.

The piezoelectric stress is the second term on the right-hand side of the first equation in Eq. (6). By taking the volumetric average of this quantity in element i in the direction of the qth PSA in the local x_3' direction it can be written as

$$T'_{33_{iq}} = \frac{1}{V_i} \int_{\Omega_i} -e'_{33_q} E'_3 \,\mathrm{d}\,\Omega \tag{39}$$

Since $e'_{13} = e'_{23} = 0$, the integrand $-e'_{33_q} E'_{33}$ can be written as $-\mathbf{1}_{33}^\top \boldsymbol{e}_q'^\top \boldsymbol{E}'$, where $\mathbf{1}_{33}$ is the vector $\{0,1,0\}^\top$ in 2D or $\{0,0,1,0,0,0\}^\top$ in 3D. Furthermore, the electric field in the local coordinate system $\boldsymbol{E}'$ can be obtained from the global coordinate system by rotating

$\boldsymbol{E}$ with $\boldsymbol{R}_{\mathrm{a}_q}$, the same rotation matrix as from Eq. (26). The electric field is related to the electric potential field $\phi(\boldsymbol{x})$ by $\boldsymbol{E} = -\nabla\phi$, where ∇ is the spatial gradient operator, so $T'_{33_{iq}}$ can be calculated as

$$T'_{33_{iq}} = \frac{1}{V_i}\int_{\Omega_i} \mathbf{1}_{33}^{\top} \boldsymbol{e}'^{\top}_q \boldsymbol{R}_{\mathrm{a}_q} \nabla\phi \,\mathrm{d}\,\Omega \tag{40}$$

With the linearity assumptions discussed in Section 2.2, the electric potential field can be written as the product of an interpolation matrix of piecewise linear functions defined in element i and a vector of the nodal electric potentials from the same element, $\boldsymbol{\phi}_i$. The gradient operator ∇ applied on the interpolation matrix yields $\boldsymbol{B}_{\phi}$ mentioned in Section 2.2, used for the calculation of the element-wise electric and piezoelectric matrices in Eq. (14). Thus, Eq. (40) becomes

$$T'_{33_{iq}} = \frac{1}{V_i}\int_{\Omega_i} \mathbf{1}_{33}^{\top} \boldsymbol{e}'^{\top}_q \boldsymbol{R}_{\mathrm{a}_q} \boldsymbol{B}_{\phi}\boldsymbol{\phi}_i \,\mathrm{d}\,\Omega = \mathbf{1}_{33}^{\top} \boldsymbol{e}'^{\top}_q \boldsymbol{R}_{\mathrm{a}_q} \boldsymbol{\zeta}\boldsymbol{\phi}_i \tag{41}$$

The simplification can be made with $\boldsymbol{\zeta} = \frac{1}{V_i}\int_{\Omega_i} \boldsymbol{B}_{\phi} \,\mathrm{d}\,\Omega$ because only $\boldsymbol{B}_{\phi}$ is a function of space. Using a homogeneous mesh, $\boldsymbol{\zeta}$ can be calculated only once.

It is known that the maximum possible stress magnitude that $T'_{33_{iq}}$ may have is

$$T'_{\max} = n\, e'_{33}\frac{|\Delta\phi|_{\max}}{\|\boldsymbol{a}_q\|} = \frac{\|\boldsymbol{a}_q\|}{t_{\mathrm{d}}}\, e'_{33}\frac{|\Delta\phi|_{\max}}{\|\boldsymbol{a}_q\|} = \frac{e'_{33}}{t_{\mathrm{d}}}|\Delta\phi|_{\max} \tag{42}$$

where e'_{33} is the e_{33} property of the constituent piezoelectric material (i.e. without any modifications based on the length of a PSA) and $|\Delta\phi|_{\max}$ is the maximum possible electric potential difference, which is known due to the electrical boundary conditions.

Thus, the sign of the piezoelectric stress in element i related to the PSA q can be calculated as

$$\Xi_{iq} = \frac{T'_{33_{iq}}}{T'_{\max}} \tag{43}$$

where $\Xi_{iq} \in [-1; 1]$. Note, however, that whether or not element i is within a PSA has not been considered yet. To do so, and in order to obtain an average value over each PSA, a weighted average of Ξ_{iq} over $V_i\rho_{p_{iq}}$ is calculated, thus yielding the average sign of the piezoelectric stress of the qth PSA

$$\bar{\Xi}_q = \frac{\sum_i^{n_{\mathrm{e}}} V_i\rho_{p_{iq}}\Xi_{iq}}{\sum_i^{n_{\mathrm{e}}} V_i\rho_{p_{iq}}} \tag{44}$$

For the actuator to push structures apart, $\bar{\Xi}_q$ has to be strictly negative for every actuator $q = 1, \ldots, n_{\mathrm{a}}$. Also, the opaqueness values α_q have to be taken into account for the polarization constraint to be ignored during the optimization process for "transparent" actuators. If $\bar{\Xi}_q$ is simply multiplied by α_q, then the sign goes to zero when $\alpha_q \to 0$, which could violate the constraint and generate designs with semi-transparent α_q. Thus, ϵ-relaxation is applied, similarly to [62–64]. The polarization constraint is therefore given by

$$g_{\mathrm{pol}} = \left(\bar{\Xi}_q + \gamma + \epsilon\right)\alpha_q - \epsilon \tag{45}$$

where $\gamma = 0.01$ in order for $\bar{\Xi}_q$ to be strictly negative and $\epsilon = 0.001$.

4.5. Sensitivities

In this subsection the sensitivities of the objective and constraint functions with respect to the design variables are derived. Since the chain rule is used, the derivatives of the equations from the preceding subsections are given in reverse order of appearance, with the exception of the derivatives of the equivalent piezoelectric material properties shown in Section 2.1 and the derivatives of all of the vectors and matrices obtained from the geometry projection method in Section 2.3, which are detailed in Appendix A.

In this section the notation specifying the mechanical $_{\mathrm{uu}}$, piezoelectric $_{\phi\mathrm{u}}$ and dielectric $_{\phi\phi}$ submatrices, SIMP exponents (w_{a}, w_{sv}, w_{cd}) and softargmax values (σ_{iq}) is omitted, with the understanding that every element matrix is composed of these submatrices, which in turn depend on their own corresponding exponents and softargmax values, to simplify notation. They are explicitly given when necessary.

The geometric variables of the qth PSA, i.e. $\boldsymbol{x}_{0_q}$, $\boldsymbol{x}_{\mathrm{f}_q}$ or d_q, are referred to as x_q. In the most general case, z is used as a universal design-variable, representing x_q, α_q, ρ_{sv_i} or ρ_{cd_i}.

Firstly, the derivative of the objective function f Eq. (35) with respect to z is

$$\frac{\partial f}{\partial z} = -\boldsymbol{\lambda}_1^{\top}\frac{\partial \boldsymbol{K}}{\partial z}\boldsymbol{U} \tag{46}$$

where $\boldsymbol{K}$ and $\boldsymbol{U}$ are the global assembled matrix and nodal values, respectively, from Eq. (12). The adjoint vector $\boldsymbol{\lambda}_1$ is obtained by solving the adjoint problem

$$\boldsymbol{K}\boldsymbol{\lambda}_1 = \begin{Bmatrix}\boldsymbol{L}\\ \boldsymbol{0}\end{Bmatrix} \tag{47}$$

where $\boldsymbol{L}$ is the vector from the definition of the objective function, Eq. (35).

Next the derivative of the global assembled matrix with respect to z has to be calculated. Its form changes depending on the type of design variable, as can be seen in the following equations. Firstly we define an auxiliary matrix $\boldsymbol{M}_{iq}$ for each element i and PSA q such that

$$\boldsymbol{M}_{iq} = \boldsymbol{K}_{\mathrm{A}_{iq}} - \rho_{\mathrm{v}_{iq}}^{w_\mathrm{a}} \boldsymbol{K}_{\mathrm{M}_i} - \sum_j^{n_\mathrm{a}} \sigma_{ij} \left(\boldsymbol{K}_{\mathrm{A}_{ij}} - \rho_{\mathrm{v}_{ij}}^{w_\mathrm{a}} \boldsymbol{K}_{\mathrm{M}_i} \right) \tag{48}$$

Then the derivatives of the mechanical $\boldsymbol{K}_{\mathrm{uu}}$ and piezoelectric $\boldsymbol{K}_{\phi\mathrm{u}}$ submatrices are calculated similarly to each other, with the difference being the values of the SIMP exponents w_a, w_sv and w_cd. Additionally, for the electrical submatrix $\boldsymbol{K}_{\phi\phi}$ the equations are slightly different, due to the different softargmax parameter $\sigma_{\phi\phi_{iq}}$. Abusing notation by referring to both $\boldsymbol{K}_{\mathrm{uu}}$ and $\boldsymbol{K}_{\phi\mathrm{u}}$ simply as $\boldsymbol{K}$, their derivatives with respect to x_q and α_q can be calculated as

$$\frac{\partial \boldsymbol{K}}{\partial x_q} = \sum_i^{n_\mathrm{e}} \frac{\partial \boldsymbol{K}_i}{\partial x_q} = \sum_i^{n_\mathrm{e}} \sigma_{iq} \left(\frac{\partial \boldsymbol{K}_{\mathrm{A}_{iq}}}{\partial x_q} - w_\mathrm{a} \rho_{\mathrm{v}_{iq}}^{w_\mathrm{a}-1} \frac{\partial \rho_{\mathrm{v}_{iq}}}{\partial x_q} \boldsymbol{K}_{\mathrm{M}_i} + \beta \alpha_q^{w_\mathrm{a}} w_\mathrm{a} \rho_{\mathrm{v}_{iq}}^{w_\mathrm{a}-1} \frac{\partial \rho_{\mathrm{v}_{iq}}}{\partial x_q} \boldsymbol{M}_{iq} \right) \tag{49}$$

$$\frac{\partial \boldsymbol{K}}{\partial \alpha_q} = \sum_i^{n_\mathrm{e}} \frac{\partial \boldsymbol{K}_i}{\partial \alpha_q} = \sum_i^{n_\mathrm{e}} \sigma_{iq} \left(\frac{\partial \boldsymbol{K}_{\mathrm{A}_{iq}}}{\partial \alpha_q} + \beta \rho_{\mathrm{v}_{iq}}^{w_\mathrm{a}} w_\mathrm{a} \alpha_q^{w_\mathrm{a}-1} \boldsymbol{M}_{iq} \right) \tag{50}$$

The sum over the number of elements n_e can be understood as an assembly procedure, with λ_1 and $\boldsymbol{U}$ in Eq. (46) being the complete nodal vectors. However, it is more straightforward to implement $\frac{\partial f}{\partial z}$ as a summation over the element-level vectors and matrices, i.e. $-\sum_i^{n_\mathrm{e}} \lambda_{1_i}^\top \frac{\partial \boldsymbol{K}_i}{\partial z} \boldsymbol{U}_i$, in which case $\frac{\partial \boldsymbol{K}_i}{\partial z}$ are the summands of Eqs. (49) and (50).

Then the derivatives of $\boldsymbol{K}_{\phi\phi}$ with respect to x_q and α_q are

$$\frac{\partial \boldsymbol{K}_{\phi\phi}}{\partial x_q} = \sum_i^{n_\mathrm{e}} \frac{\partial \boldsymbol{K}_{\phi\phi_i}}{\partial x_q} = \sum_i^{n_\mathrm{e}} \sigma_{\phi\phi_{iq}} \left(\frac{\partial \boldsymbol{K}_{\mathrm{A}_{\phi\phi_{iq}}}}{\partial x_q} + \beta \alpha_q^{w_{\mathrm{a}_{\phi\phi}}} w_{\mathrm{a}_{\phi\phi}} \rho_{\mathrm{v}_{iq}}^{w_{\mathrm{a}_{\phi\phi}}-1} \frac{\partial \rho_{\mathrm{v}_{iq}}}{\partial x_q} \boldsymbol{M}_{\phi\phi_{iq}} \right) \tag{51}$$

$$\frac{\partial \boldsymbol{K}_{\phi\phi}}{\partial \alpha_q} = \sum_i^{n_\mathrm{e}} \frac{\partial \boldsymbol{K}_{\phi\phi_i}}{\partial \alpha_q} = \sum_i^{n_\mathrm{e}} \sigma_{\phi\phi_{iq}} \frac{\partial \boldsymbol{K}_{\mathrm{A}_{\phi\phi_{iq}}}}{\partial \alpha_q} \tag{52}$$

The derivatives of $\boldsymbol{K}_{\mathrm{uu}}$, $\boldsymbol{K}_{\phi\mathrm{u}}$ and $\boldsymbol{K}_{\phi\phi}$, referred to simply as $\boldsymbol{K}$ for ease of notation, with respect to ρ_{sv_i} and ρ_{cd_i} are calculated as:

$$\frac{\partial \boldsymbol{K}}{\partial \rho_{\mathrm{sv}_i}} = \sum_j^{n_\mathrm{e}} \frac{\partial \boldsymbol{K}_j}{\partial \rho_{\mathrm{sv}_i}} = \sum_j^{n_\mathrm{e}} \left(1 - \sum_q^{n_\mathrm{a}} \sigma_{jq} \rho_{\mathrm{v}_{jq}}^{w_\mathrm{a}} \right) w_\mathrm{sv} \hat{\tilde{\rho}}_{\mathrm{sv}_j}^{w_\mathrm{sv}-1} \left(\boldsymbol{K}_{\mathrm{S}_j} - \boldsymbol{K}_\mathrm{V} \right) \frac{\partial \hat{\tilde{\rho}}_{\mathrm{sv}_j}}{\partial \tilde{\rho}_{\mathrm{sv}_j}} \frac{\partial \tilde{\rho}_{\mathrm{sv}_j}}{\partial \rho_{\mathrm{sv}_i}} \tag{53}$$

$$\frac{\partial \boldsymbol{K}}{\partial \rho_{\mathrm{cd}_i}} = \sum_j^{n_\mathrm{e}} \frac{\partial \boldsymbol{K}_j}{\partial \rho_{\mathrm{cd}_i}} = \sum_j^{n_\mathrm{e}} \left(1 - \sum_q^{n_\mathrm{a}} \sigma_{jq} \rho_{\mathrm{v}_{jq}}^{w_\mathrm{a}} \right) w_\mathrm{cd} \hat{\tilde{\rho}}_{\mathrm{sv}_j}^{w_\mathrm{sv}} \left(\hat{\tilde{\rho}}_{\mathrm{cd}_j}^{w_\mathrm{cd}-1} \boldsymbol{K}_\mathrm{C} - \left(1 - \hat{\tilde{\rho}}_{\mathrm{cd}_j} \right)^{w_\mathrm{cd}-1} \boldsymbol{K}_\mathrm{D} \right) \frac{\partial \hat{\tilde{\rho}}_{\mathrm{cd}_j}}{\partial \tilde{\rho}_{\mathrm{cd}_j}} \frac{\partial \tilde{\rho}_{\mathrm{cd}_j}}{\partial \rho_{\mathrm{cd}_i}} \tag{54}$$

where, again, care should be taken to use $\sigma_{\phi\phi_{iq}}$ for the electrical submatrix. In these equations, the sum over the elements represents the application of the derivative of the convolutional filter $\frac{\partial \tilde{\rho}_j}{\partial \rho_i}$, since this filter distributes information between neighbouring elements. In the actual implementation, the sum does not have to be performed and $\frac{\partial \tilde{\rho}_j}{\partial \rho_i}$ represents the application of the convolutional filter on the vector of size n_e obtained after calculating all other operations in the equation.

The derivative of the volume constraint g_v with respect to ρ_cd is 0. With an auxiliary variable ψ_{iq} shown in Eq. (55), the derivatives of g_v with respect to x_q, α_q and ρ_sv are given in Eq. (56).

$$\psi_{iq} = 1 + \kappa \left(\alpha_q \rho_{\mathrm{v}_{iq}} - \sum_j^{n_\mathrm{a}} \sigma_{\mathrm{v}_{ij}} \alpha_j \rho_{\mathrm{v}_{ij}} \right) \tag{55}$$

$$\begin{aligned}
\frac{\partial g_\mathrm{v}}{\partial x_q} &= \frac{\alpha_q \sum_i^{n_\mathrm{e}} V_i \sigma_{\mathrm{v}_{iq}} \left(g_\mathrm{v} + V_\mathrm{f} - \hat{\tilde{\rho}}_\mathrm{sv} \right) \psi_{iq} \frac{\partial \rho_{\mathrm{v}_{iq}}}{\partial x_q}}{\sum_i^{n_\mathrm{e}} V_i \left(1 - \sum_q^{n_\mathrm{a}} \sigma_{\mathrm{v}_{iq}} \alpha_q \rho_{\mathrm{v}_{iq}} \right)} \\
\frac{\partial g_\mathrm{v}}{\partial \alpha_q} &= \frac{\sum_i^{n_\mathrm{e}} V_i \sigma_{\mathrm{v}_{iq}} \left(g_\mathrm{v} + V_\mathrm{f} - \hat{\tilde{\rho}}_\mathrm{sv} \right) \psi_{iq} \rho_{\mathrm{v}_{iq}}}{\sum_i^{n_\mathrm{e}} V_i \left(1 - \sum_q^{n_\mathrm{a}} \sigma_{\mathrm{v}_{iq}} \alpha_q \rho_{\mathrm{v}_{iq}} \right)} \\
\frac{\partial g_\mathrm{v}}{\partial \rho_{\mathrm{sv}_i}} &= \frac{\sum_j^{n_\mathrm{e}} V_j \left(1 - \sum_q^{n_\mathrm{a}} \sigma_{\mathrm{v}_{jq}} \alpha_q \rho_{\mathrm{v}_{jq}} \right) \frac{\partial \hat{\tilde{\rho}}_{\mathrm{sv}_j}}{\partial \tilde{\rho}_{\mathrm{sv}_j}} \frac{\partial \tilde{\rho}_{\mathrm{sv}_j}}{\partial \rho_{\mathrm{sv}_i}}}{\sum_j^{n_\mathrm{e}} V_j \left(1 - \sum_q^{n_\mathrm{a}} \sigma_{\mathrm{v}_{jq}} \alpha_q \rho_{\mathrm{v}_{jq}} \right)}
\end{aligned} \tag{56}$$

The non-overlap constraint g_{no} of Eq. (38) is only a function of the geometric variables x_q and of α_q, so its derivatives with respect to the density-based variables ρ_{sv_i} and ρ_{cd_i} are 0. Its other derivatives are

$$\begin{aligned}\frac{\partial g_{\text{no}}}{\partial x_q} &= \alpha_q \sum_i^{n_\text{e}} V_i \left(H'_{\text{no}}(\alpha_q \rho_{\text{e}_{iq}}) - H'_{\text{no}}\left(\sum_j^{n_\text{a}} \alpha_j \rho_{\text{e}_{iq}} \right) \right) \frac{\partial \rho_{\text{e}_{ij}}}{\partial x_q} \\ \frac{\partial g_{\text{no}}}{\partial \alpha_q} &= \sum_i^{n_\text{e}} \rho_{\text{e}_{iq}} V_i \left(H'_{\text{no}}(\alpha_q \rho_{\text{e}_{iq}}) - H'_{\text{no}}\left(\sum_j^{n_\text{a}} \alpha_j \rho_{\text{e}_{ij}} \right) \right)\end{aligned} \tag{57}$$

Finally, for the polarization constraint g_{pol} Eq. (45), we firstly define an auxiliary term ω_q

$$\omega_q = \frac{\alpha_q}{T'_{\max} \sum_j^{n_\text{e}} \rho_{\text{p}_{jq}} V_j} \tag{58}$$

Then the derivatives of the polarization constraint with respect to the design variables are

$$\begin{aligned}\frac{\partial g_{\text{pol}}}{\partial x_q} &= \omega_q \sum_i^{n_\text{e}} \left[\left(T'_{33_{iq}} - \bar{\Xi}_q T'_{\max} \right) \frac{\partial \rho_{\text{p}_{iq}}}{\partial x_q} + \rho_{\text{p}_{iq}} \mathbf{1}_{33}^\top \left(\frac{\partial \boldsymbol{e}'^\top_q}{\partial x_q} \boldsymbol{R}_{\text{a}_q} + \boldsymbol{e}'^\top_q \frac{\partial \boldsymbol{R}_{\text{a}_q}}{\partial x_q} \right) \boldsymbol{\zeta} \boldsymbol{\phi}_i \right] - \lambda_{1+q}^\top \frac{\partial \boldsymbol{K}}{\partial x_q} \boldsymbol{U} \\ \frac{\partial g_{\text{pol}}}{\partial \alpha_q} &= \bar{\Xi}_q + \gamma + \epsilon - \lambda_{1+q}^\top \frac{\partial \boldsymbol{K}}{\partial \alpha_q} \boldsymbol{U} \\ \frac{\partial g_{\text{pol}}}{\partial \rho_{\text{sv}_i}} &= -\lambda_{1+q}^\top \frac{\partial \boldsymbol{K}}{\partial \rho_{\text{sv}_i}} \boldsymbol{U} \\ \frac{\partial g_{\text{pol}}}{\partial \rho_{\text{cd}_i}} &= -\lambda_{1+q}^\top \frac{\partial \boldsymbol{K}}{\partial \rho_{\text{cd}_i}} \boldsymbol{U}\end{aligned} \tag{59}$$

where the adjoint vectors λ_{1+q} are obtained by solving the following adjoint problem for each PSA q

$$\boldsymbol{K} \lambda_{1+q} = \left\{ \begin{matrix} \mathbf{0} \\ \omega_q \sum_i^{n_\text{e}} \rho_{\text{p}_{iq}} V_i \left(\mathbf{1}_{33}^\top \boldsymbol{e}'^\top_q \boldsymbol{R}_{\text{a}_q} \boldsymbol{\zeta} \right)^\top \end{matrix} \right\} \tag{60}$$

From an implementation perspective, note that the right-hand sides of the adjoint problems shown in Eqs. (47) and (60) are independent of the solution of the state equations, i.e. $\boldsymbol{U}$. This means that all of these right-hand sides can be stacked together with the right-hand side of the state equation (12) and only one linear system has to be solved per iteration of the optimization problem, solving simultaneously for $\boldsymbol{U}$ and λ_j, where $j = 1, \dots, 1 + n_\text{a}$.

4.6. Optimization flowchart

Fig. 10 shows a flowchart of the optimization procedure. At the start of the algorithm, the initial values of the geometric ($\boldsymbol{x}_0$, $\boldsymbol{x}_\text{f}$, d and α) and density-based (ρ_{sv} and ρ_{cd}) design variables are specified, together with the material properties and the optimization parameters. Next, the iterative loop starts, with the convolutional filter and Heaviside projection applied to the density-based design variables, yielding $\hat{\bar{\rho}}_{\text{sv}}$ and $\hat{\bar{\rho}}_{\text{cd}}$. Then the geometric design variables are used to calculate the pseudo-densities that describe the material regions within the PSA ρ_v, ρ_e and ρ_v, following Eqs. (15) to (24).

The element-level stiffness matrices are then calculated as in Eq. (34), which after the assembly procedure yield the global stiffness matrix $\boldsymbol{K}$ from Eq. (13). This equation is solved to find the nodal displacements $\boldsymbol{u}$ and electric potentials $\boldsymbol{\phi}$, which are used to calculate the objective and constraint functions presented in Eq. (35).

At this point in the algorithm, the convergence and the stopping criteria are evaluated. If both are not met, the sensitivities are calculated as presented in Section 4.5 and the results are passed to the subsolver of the optimization algorithm, i.e. the MMA. The design variables are updated and a new iteration begins. When either of the aforementioned criteria is met, the optimization is finalized.

4.7. Optimization approach

The optimization problem posed in Eq. (35) was solved using a nested analysis and design approach, wherein at each iteration of the design process the equilibrium Eqs. (12) are solved, the objective and constraint functions are evaluated, their sensitivities are calculated and new values are ascribed to the design variables $\boldsymbol{x}_{0_q}$, $\boldsymbol{x}_{\text{f}_q}$. d_q and α_q for $q = 1, \dots, n_\text{a}$, as well as ρ_{sv_i} and ρ_{cd_i} for $i = 1, \dots, n_\text{e}$.

As previously mentioned, the MMA is used as the optimization algorithm. For the considered problem with diverse design variables, it was found that additional care must be taken in ensuring the stability of the optimization. For the MMA, the geometric design variables are normalized to be within 0 and 1, as done in [43]. The move limits of the geometric design variables and α were set to 0.01 and the move limits of the density-based variables to 0.08, based on initial experiments. Additionally, from the note published by Svanberg [65], the c parameter was set to 10^6. For lower values of c the volume and maximum length constraints become frequently violated in the initial iterations of the optimization process.

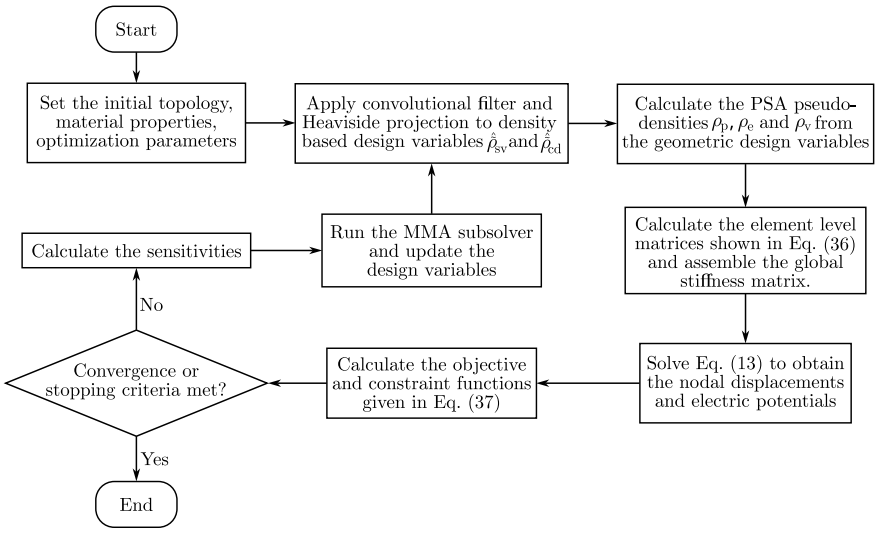

Fig. 10. Flowchart of the optimization algorithm.

The values of the objective and constraint functions are normalized at each iteration of the design process for the MMA. The initial normalization value of the objective function f_0 is calculated based on the maximum theoretical output of a 1D PSA bar. It is:

$$f_0 = 10^{\lfloor \log_{10} d'_{33} n_{\max} |\Delta\phi|_{\max} \rfloor} \tag{61}$$

where d'_{33} is the piezoelectric property of the constituent material in strain-charge form, $n_{\max} = \frac{L_{\max}}{t_d}$ is the maximum number of layers in the PSA during the optimization, $|\Delta\phi|_{\max}$ is the maximum applied voltage difference at the boundaries, and $\lfloor\cdot\rfloor$ is the floor function. Then the ratio $\frac{f}{f_0}$ is checked every 30 iterations: if $\frac{f}{f_0} < 0.1$, f_0 is divided by 10; else if $\frac{f}{f_0} > 100$, f_0 is multiplied by 10; otherwise f_0 remains unchanged. The normalization values of the constraints g_v, g_{no} and g_{pol} are 0.01, $\frac{h^2}{20}$ and 0.1, respectively. The maximum length constraints of the PSAs are normalized by dividing by $\frac{L_{\max}}{10}$ and the minimum length constraints by dividing by $\frac{L_{\min}}{10}$.

A continuation approach is used for the Heaviside sharpness parameter β of Eq. (30), starting from 0.05 and increasing in 4% every iteration until it reaches 80. A direct solver was applied for the solution of the linear systems to obtain the results shown in the subsequent section.

5. Results

5.1. Inverter-like mechanism

The methods presented in this subsection were applied to the inverter-like mechanism shown in Fig. 11. Its dimensions are 0.10×0.05 m^2 and its domain was discretized with $400 \times 200 = 80\,000$ elements. A spring of stiffness $k = 10^9$ $\frac{\text{N}}{\text{m}}$ is attached to the horizontal degree of freedom of the upper-right node, which will have its displacement minimized. Furthermore, a non-design domain of 5×2.5 mm^2 is considered in the upper-right corner, made of solid dielectric material. A maximum solid fraction of $V_f = 25\%$ of the design domain is set. The rest of the domain is initialized with $\rho_{sv_i} = \rho_{cd_i} = 0.23$ for all elements $i = 1, \ldots, n_e$, to account for the small rectangular non-design domain and start the optimization with a feasible volume. The number of PSAs and their initial positions, sizes and orientations are given in each of the following subsections. In all cases the radius of the density filter was 2 mm. The piezoelectric disc thickness was constant equal to $t_d = 0.5$ mm. The offset parameters were $l' = 6h$ and $d' = 8h$.

The bottom one-third of left surface is grounded, while the upper one-third has a prescribed non-zero voltage equal to 100 V. The minimum and maximum PSA lengths are 5 mm and 30 mm, respectively, and the minimum and maximum PSA widths are 2 mm and 10 mm, respectively. The initial values of the length and width are 15 mm and 5 mm, respectively, and an initial α_q value of 0.5, in all cases except for a benchmark problem. The softargmax sharpness parameter for the geometry projection method was $\kappa = 50$.

The dielectric material has the same mechanical properties of steel, a Young's modulus of 200 GPa and a Poisson's ratio of 0.29, but with the dielectric permittivity of air, i.e. $8.9073 \cdot 10^{-12}$ $\frac{\text{F}}{\text{m}}$. The conductive material is slightly less stiff, with a Young's modulus of 190 GPa, to encourage the optimization process to only use conductive material where necessary, a Poisson's ratio of 0.29 and a large absolute permittivity of $8.9073 \cdot 10^{-3}$ $\frac{\text{F}}{\text{m}}$, i.e. 10^9 larger than that of air. Void material has the permittivity of air, Poisson's ratio

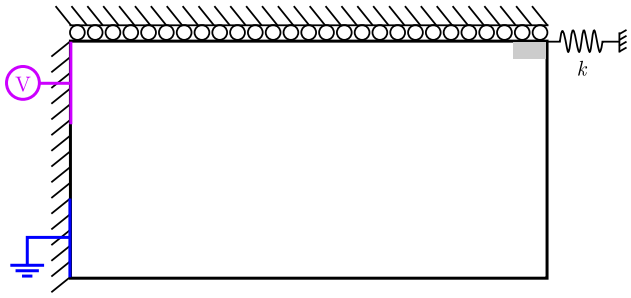

Fig. 11. General design of the inverter-like mechanism.

of steel but a Young's modulus of 200 Pa, i.e. 10^{-9} that of the dielectric material. All of these materials have 0 piezoelectricity. The elasticity, piezoelectricity and dielectric permittivity matrices of the electrode and piezoelectric materials are given in Appendix B.

The SIMP penalization exponents for the mechanical, piezoelectric and electric properties are given in brackets in that order. They are $\boldsymbol{w}_{\mathrm{a}} = [3,3,3]$, $\boldsymbol{w}_{\mathrm{sv}} = [3,3,2]$ and $\boldsymbol{w}_{\mathrm{cd}} = [3,3,2]$. The optimization stops either when the average change in the design variables is lower than 10^{-4} or when 300 iterations are reached.

In the figures illustrating the topologies, $\hat{\tilde{\rho}}_{\mathrm{cd}}^{w_{\mathrm{cd_{uu}}}}$ is shown. Only solid elements are shown by thresholding $\hat{\tilde{\rho}}_{\mathrm{sv}} \geq 0.5$. For the illustration of the displaced structure, post-processing is applied to smoothen the design by firstly converting element-level values to nodal ones and then thresholding the solid–void regions with a value of 0.5. Additionally, in all figures the components of the PSAs are illustrated by thresholding ρ_q at 0.5, where ρ_q here can be any of the geometric pseudo-densities of Section 2.3. The solid piezoelectric region is coloured with a white to green gradient, since $\alpha_q \rho_{\mathrm{p}_{iq}}$ can hold values between 0 and 1. A grey arrow shows the polarization direction of the PSA. Similarly, the electrode regions are coloured with a white to yellow gradient.

The method was implemented in Python, a high-level general-purpose programming language, with some wrapped C components. The Intel PARDISO solver of the Intel oneAPI Math Kernel Library [66] was used as the linear system solver, a free to use and free to redistribute software, according to Intel's Simplified Software License (Version October 2022). Each iteration of the algorithm for the considered mesh of 80 000 elements takes on average 3 s on a desktop computer with an Intel i9-9900KF CPU. Since performance was not the focus of this study, future works may improve on this by, e.g.: using more sophisticated and efficient solvers, such as multigrid [67]; adapting the code to run in more performant hardware, such as a cluster with GPUs [68] and/or FPGAs; using commercial instead of free software and programming languages.

5.1.1. Benchmark result — fixed PSA geometry

In this subsection, a design obtained from only optimizing for the solid–void and conductive–dielectric material distributions of the underlying compliant mechanism is shown, considering a fixed location and geometry for a single PSA. The length and diameter of the PSA are equal to the maximum values for the more general cases, i.e. 30 mm and 10 mm, respectively, and $\alpha = 1$. The PSA is centred in the design domain with a rightwards polarization direction, as shown in Fig. 12.

The final topology obtained from the optimization process is shown in Fig. 13(a), with dielectric material in blue and conductive material in red. The entire solid region is load-bearing, with conductive material being mostly utilized to connect the PSA to the prescribed voltages, and dielectric material where the electrical connections are not required.

The displacements are magnified by a factor of 2000 and the displaced structure is shown in Fig. 13(b). The undeformed configuration is shown in light grey in the background. Dielectric material is shown in dark grey, while a red to blue colour scheme shows the voltage distribution on the conductive material. It can be seen that the voltages in the conductive material seem to be either 0 V or 100 V, as expected, due to the large permittivity values used to model the conductive material. Furthermore, the design works as intended, moving the upper right-most corner to the left.

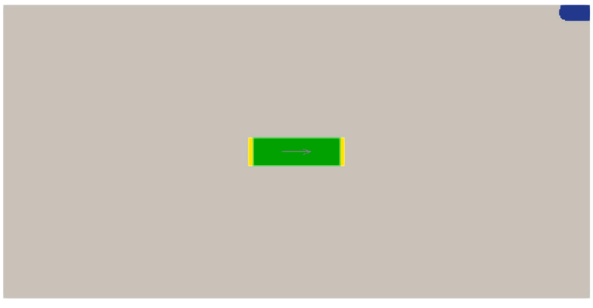

Fig. 12. Initial design for one PSA. The grey area has $\rho_{sv} = \rho_{cd} = 0.23$.

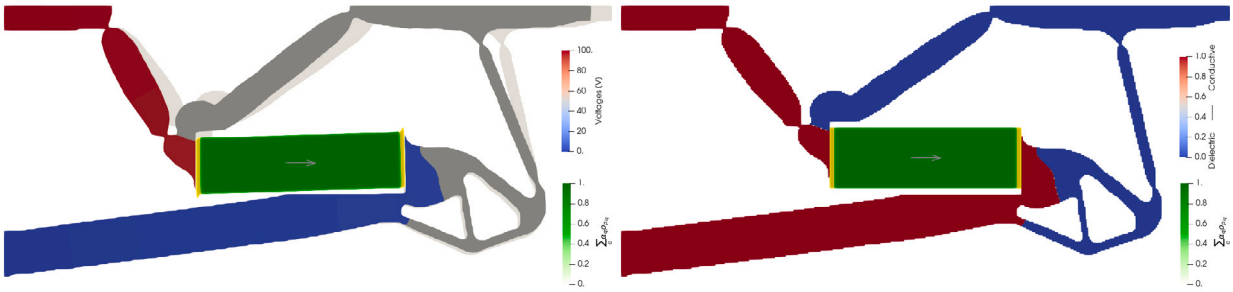

(a) $\hat{\rho}_{\text{sv}} \geq 0.5$ and distribution of $\hat{\rho}_{\text{cd}}^{u'_{\text{cd}_{\text{uu}}}}$.

(b) Voltage distribution in the conductive material of the displaced structure (magnified by a factor of 2000).

Fig. 13. Final topology of the benchmark problem with fixed PSA geometry, position and orientation. (For interpretation of the references to colour in this figure legend, the reader is referred to the web version of this article.)

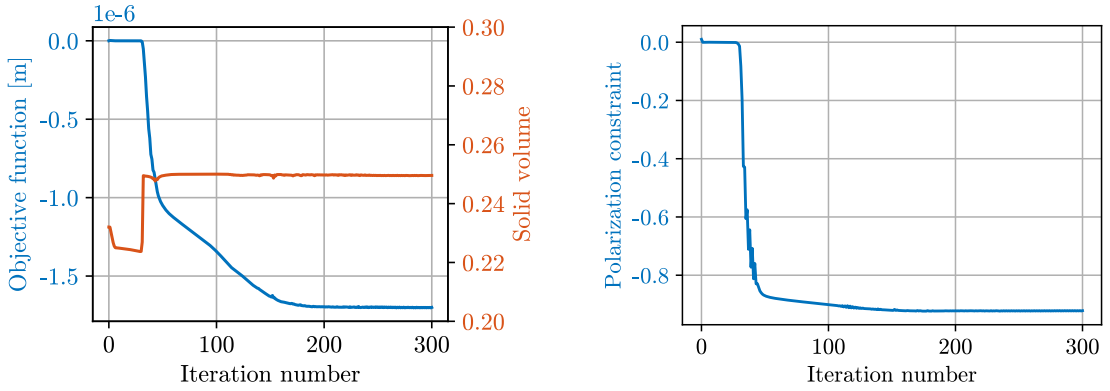

Fig. 14. Optimization history of the benchmark problem.

The convergence histories are depicted in Fig. 14. Smooth and steady convergence is observed, the volume constraint is active while the polarization constraint is only active in the initial iterations. A final value of the objective function of $-1.7003 \cdot 10^{-6}$ m was obtained.

5.1.2. Single PSA

In this subsection, a result is presented with the complete optimization problem for one PSA. Similarly to the previous subsection, the PSA is initially centred in the design domain with a rightwards polarization direction as illustrated in Fig. 12, although now with $\alpha = 0.5$, an initial diameter of 5 mm and an initial length of 15 mm.

The final topology can be seen in Fig. 15. The orientation of the PSA in the final design rotated in 58.95 deg in the clock-wise direction. The length and the diameter of the PSA are equal to their maximum allowable values, i.e. 30 mm and 10 mm, respectively, with $\alpha = 1$. This was expected, since a thicker PSA has a larger blocking force and a longer PSA has a larger stroke, especially considering piezoelectric layers of constant thickness.

The convergence histories can be seen in Fig. 16. Similar behaviour as in the benchmark example is observed, indicating that the chosen variable scaling is effective. The polarization constraint again is inactive in all but the first iterations. The objective function decreased smoothly until the optimization converged in iteration 227, reaching a value of $-2.4930 \cdot 10^{-6}$ m, 46.64% better than the benchmark problem.

5.1.3. The importance of the polarization constraint

If the problem shown in the previous subsection is optimized without considering the proposed polarization constraint, the topology shown in Fig. 17 is obtained. As can be seen from the displaced structure in Fig. 17(b), the PSA is under tension, pulling two structural regions together, which is not desirable.

The design was obtained in 290 iterations with an objective function value of $-2.6311 \cdot 10^{-6}$ m, i.e. even lower than the previous case. The better objective function is expected, since in this configuration less energy is used for the elastic deformation of the

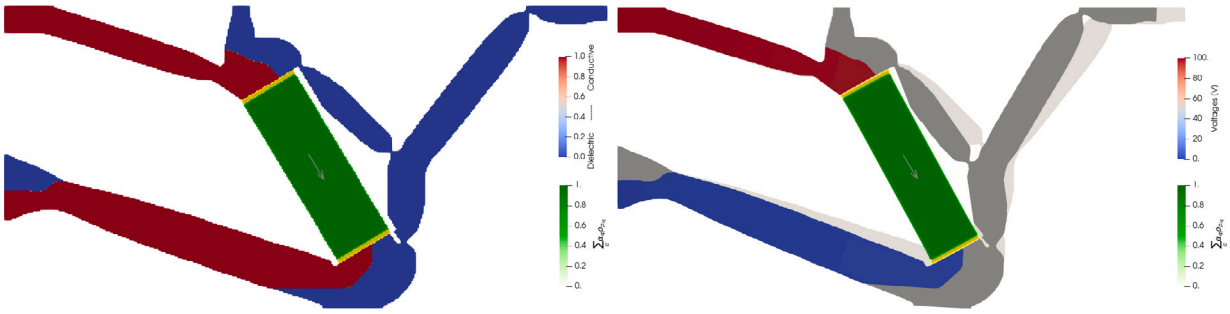

(a) $\hat{\rho}_{sv} \geq 0.5$ and distribution of $\hat{\rho}_{cd}^{w_{cd_{uu}}}$.

(b) Voltage distribution in the conductive material of the displaced structure (magnified by a factor of 2000).

Fig. 15. Final topology of the single PSA problem.

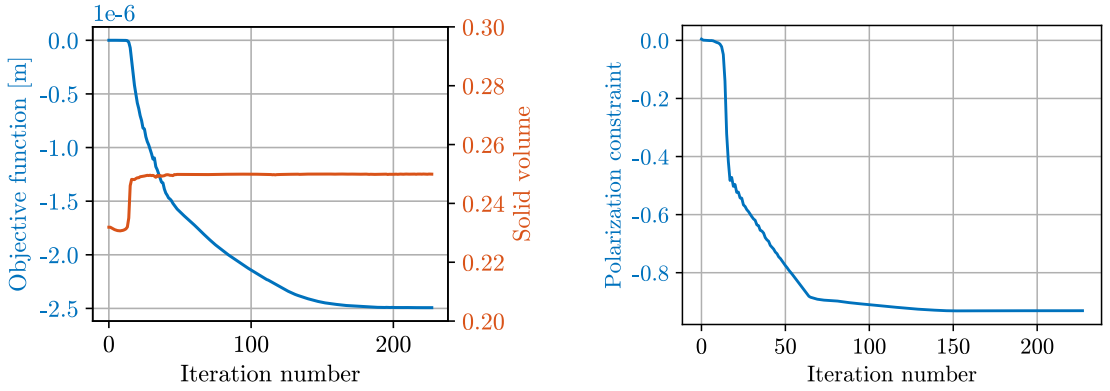

Fig. 16. Optimization history of the single PSA problem.

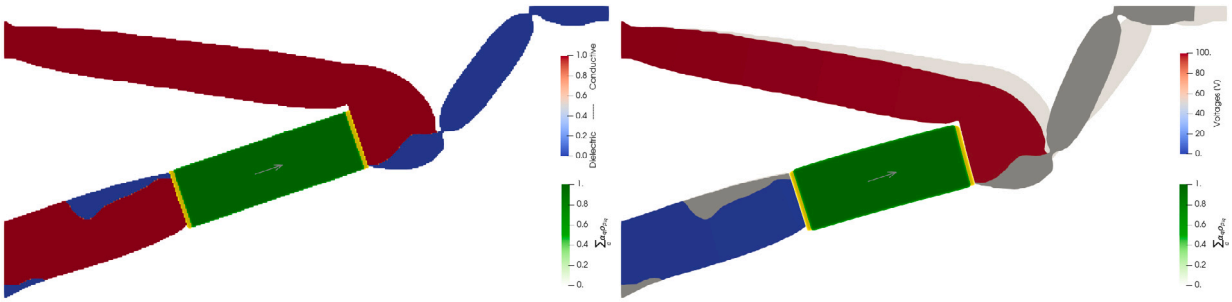

(a) $\hat{\rho}_{sv} \geq 0.5$ and distribution of $\hat{\rho}_{cd}^{w_{cd_{uu}}}$.

(b) Voltage distribution in the conductive material of the displaced structure (magnified by a factor of 2000).

Fig. 17. Final topology without polarization constraint.

underlying mechanism in comparison to the design when the PSA is in compression. We can conclude that the polarization constraint is essential to guide the design to an optimized solution based on a PSA in compression, even when it is inactive in most iterations.

5.1.4. Larger conductive permittivity

The choice of the permittivity value for the conductive and electrode materials influences the behaviour of the optimization procedure. Since a comprehensive study of the influence of this parameter on the final obtained designs is out of scope for this paper, in this section only one example showing this influence is presented. Specifically, the ϵ^S values shown in Appendix B were multiplied by 100.

Different from the previous results, the conductive material is used sparingly, as can be seen in the final optimized design in Fig. 18(b). The thin conductive material seems to describe electrical wires connecting the PSA to the electrical boundary regions. By looking at the solid–void distribution $\hat{\rho}_{sv}$ in Fig. 18(a), it can be seen that the conductive materials in the "wires" exist in grey

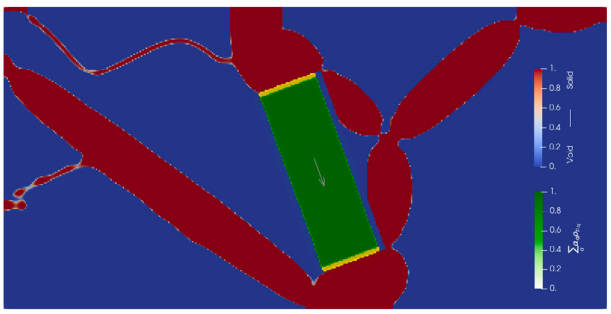

(a) Distribution of $\hat{\rho}_{sv}$.

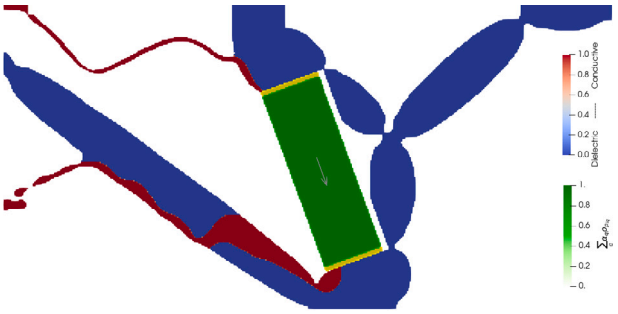

(b) $\hat{\rho}_{sv} \geq 0.5$ and distribution of $\hat{\rho}_{cd}^{u_{cd_{uu}}}$. The seemingly "disconnected wires" appear due to the low density regions seen in Fig. 18(a).

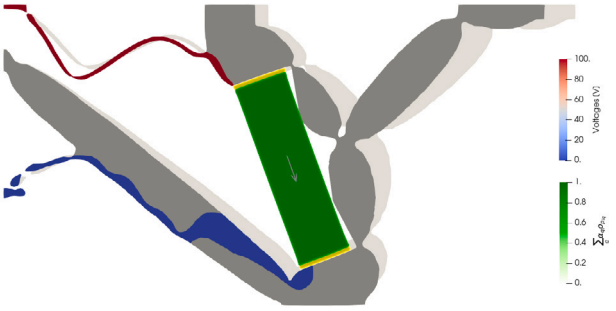

(c) Voltage distribution in the conductive material of the displaced structure (magnified by a factor of 2000).

Fig. 18. Final topology for a higher permittivity value of conductive and electrode materials.

regions, thus exhibiting low mechanical stiffness. Despite having intermediate solid–void values ρ_{sv}, the conductivity is still quite large, since the permittivity of the conductive material in this example is 7 orders of magnitude larger than that of the piezoelectric material. Fig. 18(c) shows the deformed structure. The final length and diameter of the PSA are equal to the largest admissible values, i.e. 30 mm and 15 mm, respectively.

The final objective value was $-2.6658 \cdot 10^{-6}$ m, which is better than the previous result obtained for a single PSA, since the conductive material applied here is a better conductor. Thus, there are less electrical losses in the conductive material, which means that there is a larger electric potential difference between the electrodes of the PSA.

5.1.5. No equivalent piezoelectric properties

Without the equivalent piezoelectric properties for the PSA shown in Section 2.1, the optimization design problem will fail to mimic the physical behaviour of a PSA. The maximum possible piezoelectric stress within a finite element, i.e. T'_{max}, will depend on the minimum length of the PSA instead of its maximum length, since, for a fixed maximum voltage difference $|\Delta\phi|_{max}$, the electric field E'_3 within the PSA will be largest when the distance between the electrodes is smallest, L_{min}. Thus, in this case, T'_{max} will be:

$$T'_{max} = e'_{33} \frac{|\Delta\phi|_{max}}{L_{min}} \tag{62}$$

additionally, the normalization parameter of the objective function f_0 is calculated similarly to Eq. (61), but with $n_{max} = 1$.

Furthermore, for the conductive material to behave the same as in the three initial examples, the permittivity values of the conductive and electrode materials have to be scaled based on the relationship between the equivalent permittivity $\epsilon^S_{PSA_{33}}$ and that of the piezoelectric material ϵ^S_{33}, as in Eq. (11). Since $L_{max} = 30$ mm and $t_d = 0.5$ mm, then $n = 60$ and the previous values of the conductive and electrode permittivities have to be divided by $n^2 = 3600$.

The final topology and displaced structure obtained for these settings can be seen in Fig. 19. The length of the actuator is 24.7304 mm and its final width is 6.5415 mm.

The final design converged in 261 iterations and the value of the objective function was $-2.9334 \cdot 10^{-8}$ m, two orders of magnitude worse than before. This was expected, since a monolithic piezoelectric material will not be able to produce the same actuation as the PSA composed of multiple discs, given a fixed input voltage.

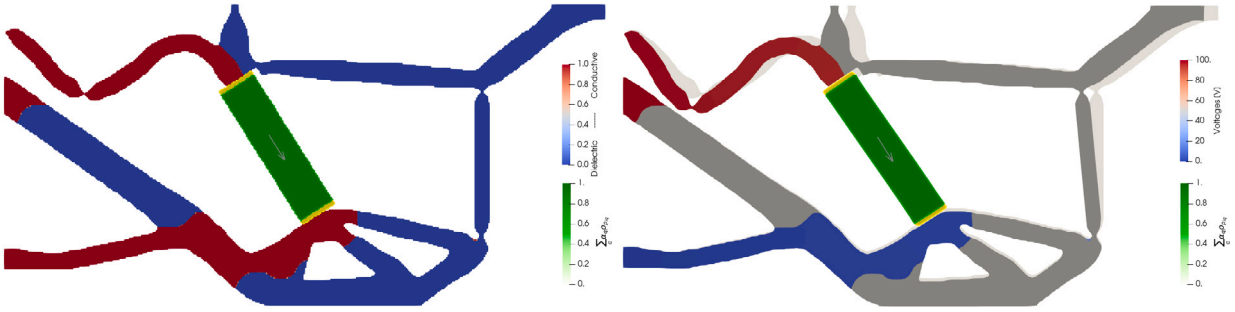

(a) $\hat{\tilde{\rho}}_{\text{sv}} \geq 0.5$ and distribution of $\hat{\tilde{\rho}}_{\text{cd}}^{u_{\text{cd}_{\text{uu}}}}$.

(b) Voltage distribution in the conductive material of the displaced structure (magnified by a factor of 80000).

Fig. 19. Final topology without the proposed equivalent piezoelectric material property for the actuator.

Fig. 20. Initial configuration for two PSAs. The grey area has $\rho_{su} = \rho_{cd} = 0.23$, as in the preceding results.

5.1.6. *Two PSAs and the effect of γ*

In this subsection, four different topologies are shown, considering two PSAs with either downward or upward polarization directions and two different values of γ, which is the parameter in the polarization constraint shown in Eq. (45) that enforces strict inequality of the average piezoelectric stresses in each PSA. The initial design is shown in Fig. 20, where the polarization directions may be both downward or both upward.

The final designs are shown in Fig. 21. For the case where the PSAs are initially oriented downwards, a value of $\gamma = 0.01$ causes one of the two PSAs to vanish for the polarization constraint to be satisfied and the final value of the objective function is similar to that of the design with one PSA. By increasing γ to 0.5, the optimization process is able to find a local optimum where both PSAs can be used under compression, thus yielding a better objective function value. For the case where the PSAs are initially oriented upwards, a value of $\gamma = 0.01$ has the same effect as before, yielding a final design where one of the PSAs vanishes and the value of the objective function is similar to that of one PSA. However, the result obtained with $\gamma = 0.5$ in this case did not inhibit the vanishing of one PSA and it yielded a slightly worse objective function value, as can be seen in the captions on Fig. 21.

5.1.7. *Two overlapping PSAs*

Finally, a result is shown where two PSAs are initially overlapping. Fig. 22 shows the initial topology. Since the initial value of α_q is 0.5 for both PSAs, the dark green region where both PSAs intersect each other has a sum $\sum_q^{n_a} \alpha_q \rho_{\text{p}_{iq}}$ for each element i equal to 1.0 and the lighter green regions have this sum equal to 0.5.

The final design can be seen in Fig. 23. It converged in 243 iterations to an objective function value of $-2.3240 \cdot 10^{-6}$ m. It can be seen that both PSAs are solid ($\alpha_q = 1$), however, the smaller PSA has both of its ends connected to the same conductive material. This occurs because there is enough of a voltage gradient in the conductive material such that the polarization constraint is satisfied and a small improvement on the objective function can be obtained.

Fig. 24 shows the non-overlap constraint g_{no} during the iterations of the optimization process. It is initially slightly positive, but quickly becomes feasible with a small decrease of α_q and is never again violated.

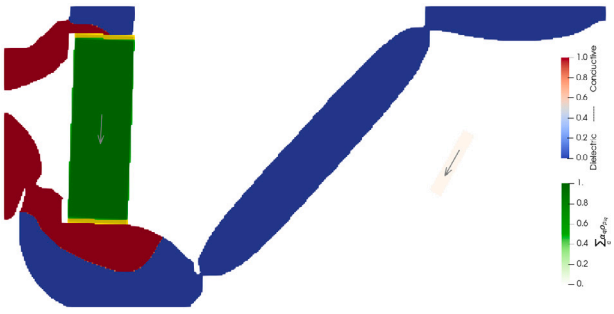

(a) Downwards with $\gamma = 0.01$. $f = -2.7346 \cdot 10^{-6}$ m.

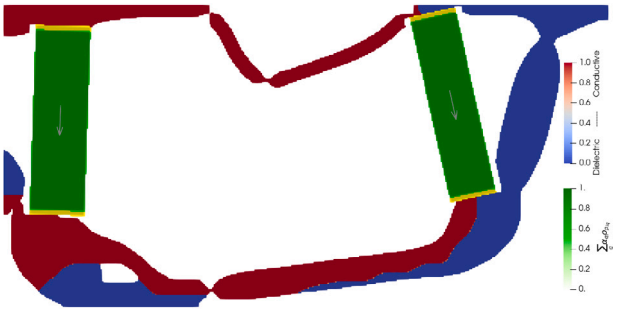

(b) Downwards with $\gamma = 0.5$. $f = -3.0542 \cdot 10^{-6}$ m.

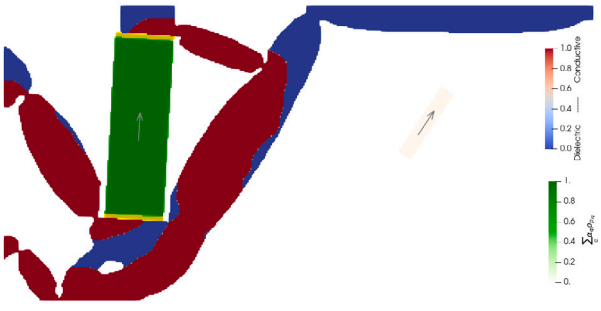

(c) Upwards with $\gamma = 0.01$. $f = -2.6837 \cdot 10^{-6}$ m.

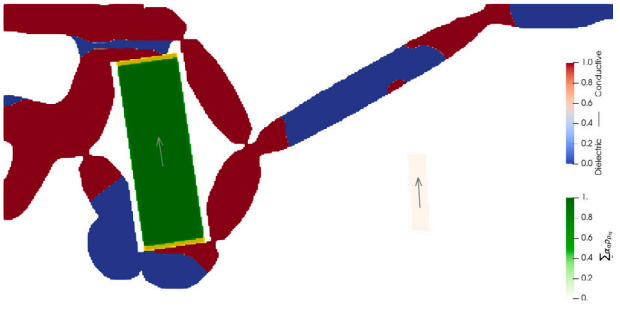

(d) Upwards with $\gamma = 0.5$. $f = -2.4046 \cdot 10^{-6}$ m.

Fig. 21. Final topologies obtained for two PSAs considering two different initial orientations and two different γ values. The objective function value f is shown for each design.

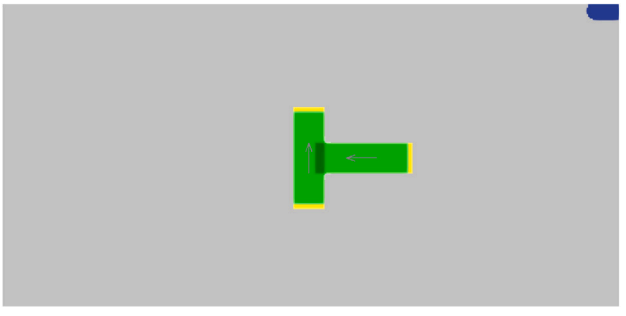

Fig. 22. Initial design of overlapping PSAs.

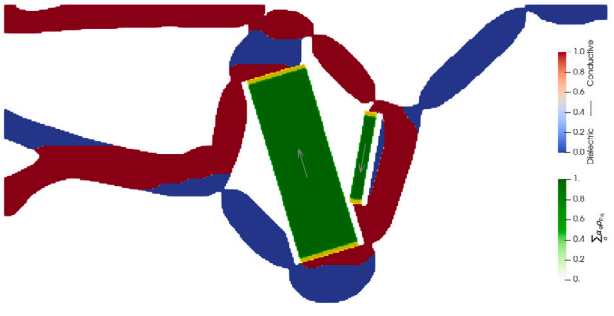

(a) $\hat{\bar{\rho}}_{sv} \geq 0.5$ and distribution of $\hat{\bar{\rho}}_{cd}^{w_{cd_{ini}}}$.

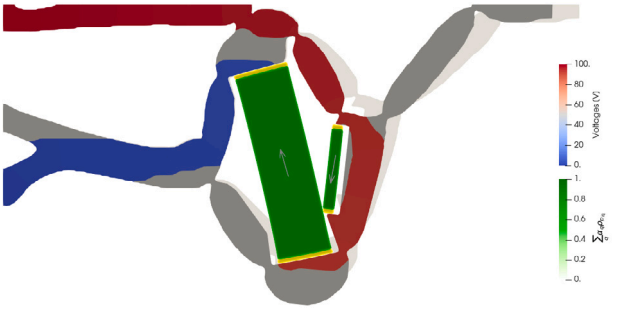

(b) Voltage distribution in the conductive material of the displaced structure (magnified by a factor of 2000).

Fig. 23. Final topology for the initially overlapping PSAs.

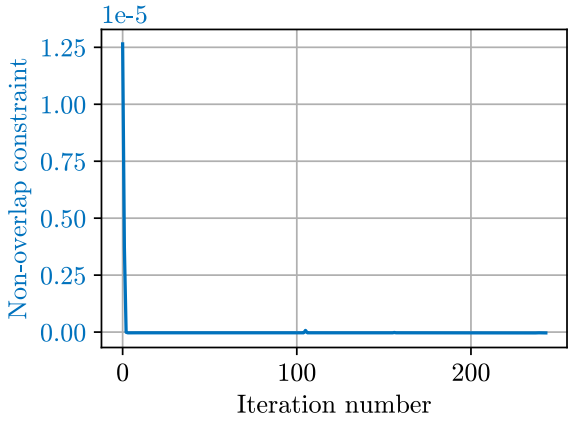

Fig. 24. Non-overlap constraint g_{no} history.

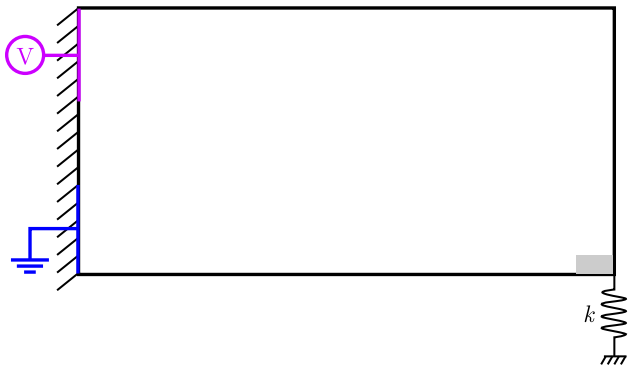

Fig. 25. General design of the cantilever mechanism.

5.2. Cantilever mechanism

The proposed method was also applied for the design of a cantilever mechanism illustrated in Fig. 25, which is clamped on the left-hand side, has the same electrical boundary conditions as the inverter-mechanism and the objective is to maximize the upward vertical displacement of the lower-right tip, which is connected to a workpiece stiffness k. Problems of this kind could be encountered in the design of precision positioning mechanisms for e.g. optical components. The material properties and optimization parameters are taken from the previous results. Multiple initial conditions are explored considering both one and two PSAs, with both the initial and optimized topologies shown in Fig. 26. Specifically for the design of Fig. 26a, the convergence and displaced structure can be seen in Fig. 27.

In general, it can be seen that the initial configuration is highly influential on the final design, which is expected, since a gradient based optimizer such as the MMA can only converge to a local optimum and is consistent with other results from literature [36,39,69]. Furthermore, the additional sizing and "opacity" variables in this work can cause more local optima to exist in comparison to the cited references. For example, in Fig. 26 it can be seen that topologies with two PSAs yield better optima than one PSA when both actuators can be fully utilized for the maximization of the desired output displacement. The best and worst obtained designs differ by a factor of 1.67 in performance, which is significant and a result of the non-convexity of the problem. Therefore, the exploration of multiple initial configurations is recommended in order to find better optimized designs.

6. Conclusion

The paper proposes a unified multiphysics framework combining multi-material density-based topology optimization and a composite multi-layered geometry-projection method to find optimized designs of smart structures composed of piezoelectric stack actuators (PSAs) modelled as having continuum equivalent piezoelectric geometry-dependent properties embedded within conductive load-bearing structures. Furthermore, a novel polarization constraint was defined that successfully inhibits undesirable designs which are improper for the use of PSAs.

Nineteen numerical examples were provided and discussed, demonstrating the capabilities of the proposed design methodology. As shown in the benchmark problem, *a priori* fixing the position, size and orientation of the actuators in the optimization process may

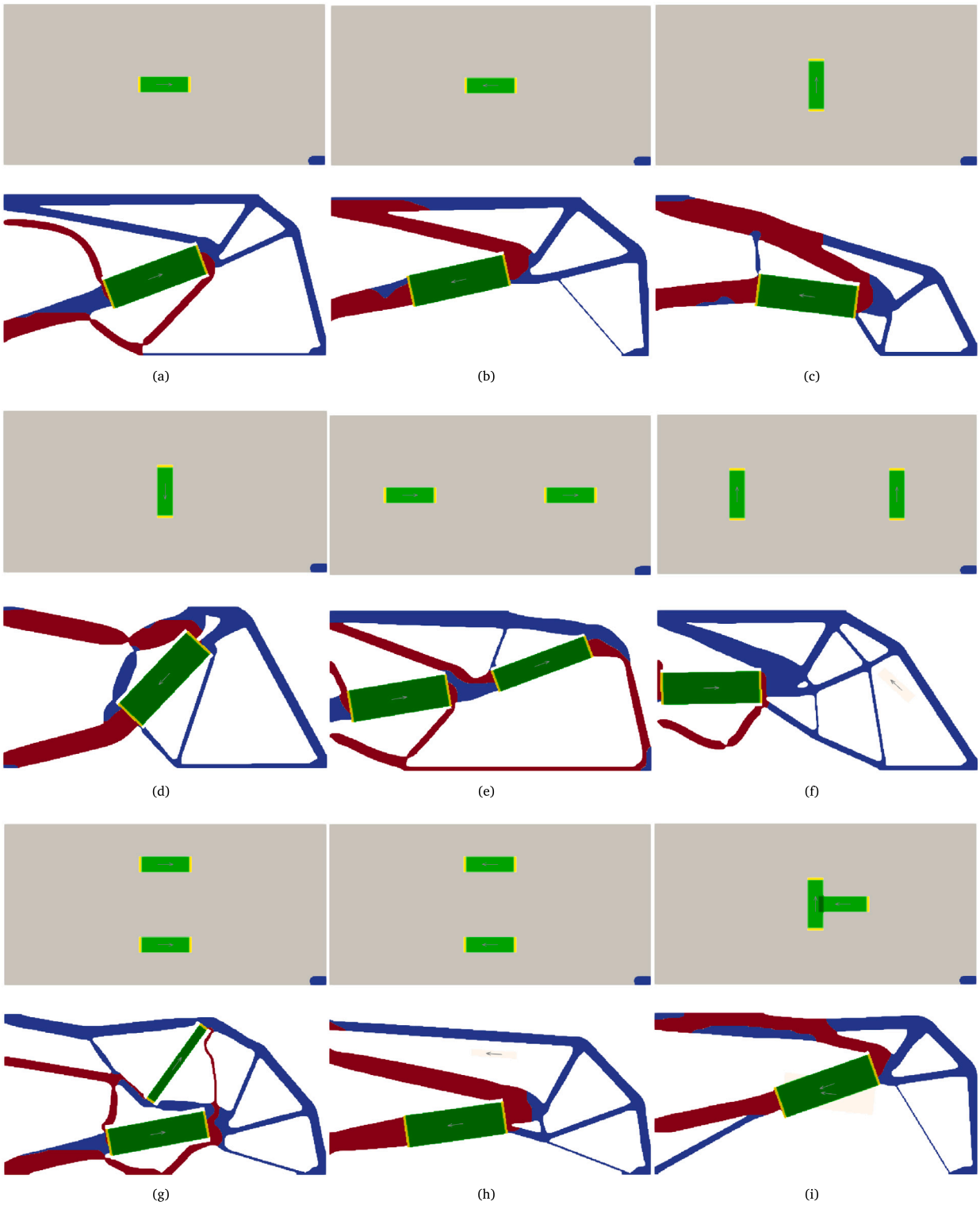

Fig. 26. Initial (top) and optimized (bottom) results for multiple cantilever mechanism configurations. Red regions are conductive and blue are dielectric. The final objective function values are (a) −1.8341 μm, (b) −2.2156 μm, (c) −2.0717 μm, (d) −2.2110 μm, (e) −3.0611 μm (best), (f) −2.3476 μm, (g) −2.0809 μm, (h) −2.3088 μm, (i) −2.0862 μm.. (For interpretation of the references to colour in this figure legend, the reader is referred to the web version of this article.)

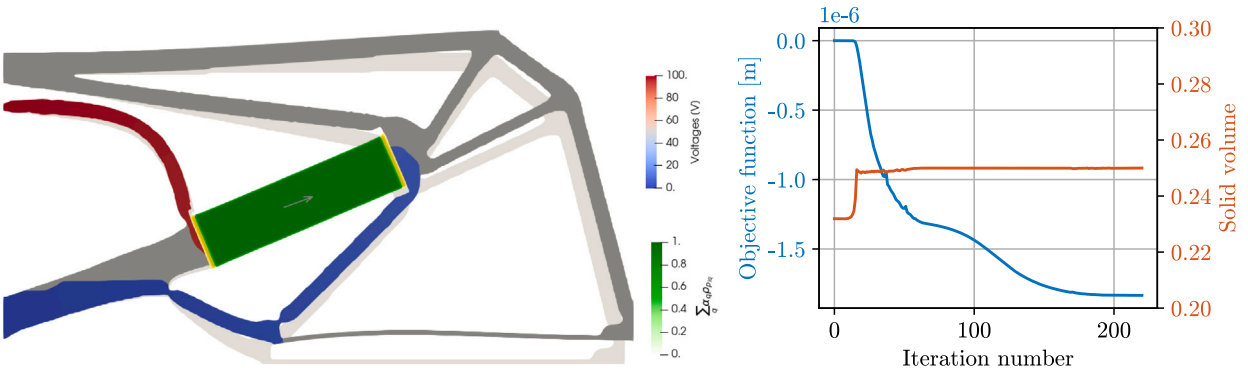

Fig. 27. Displaced structure (left, magnified by a factor of 2000) and convergence history (right) of the result shown in Fig. 26a.

lead to suboptimal designs. The proposed methodology is capable of yielding designs of smart structures with embedded actuators exclusively under compression, while allowing for the overlap of grey actuators during the optimization process. The main drawback of the method is its susceptibility to local optima, which can commonly be seen in literature for feature-mapping based methods. Exploration of multiple initial configurations and problem parameters is recommended to reduce the likelihood of obtaining inferior local optima, as demonstrated for the cantilever mechanism design problem.

We have not considered stress constraints in the smart structure optimization, as this was not the focus of this study. This however results in typical thin flexures, that may be hard to produce and prone to failure. Extending the problem formulation with adequate stress constraints, also regarding the material interfaces, is identified as a topic for future research. Additional topics for future works include non-linear effects inherent in piezoelectric actuators subject to higher input voltages; dynamic inputs for the application in vibration suppression and energy harvesting; simultaneous optimization of control parameters, broadening the scope to realize the design of a fully coupled smart structure; and extension to 3D.

CRediT authorship contribution statement

Breno Vincenzo de Almeida: Writing – original draft, Visualization, Validation, Software, Resources, Methodology, Investigation, Funding acquisition, Formal analysis, Data curation, Conceptualization. **Renato Pavanello:** Writing – review & editing, Supervision, Resources, Funding acquisition. **Matthijs Langelaar:** Writing – review & editing, Supervision, Resources, Project administration, Methodology, Investigation, Conceptualization.

Declaration of competing interest

The authors declare that they have no known competing financial interests or personal relationships that could have appeared to influence the work reported in this paper.

Data availability

No data was used for the research described in the article.

Acknowledgements

The authors are grateful to the São Paulo Research Foundation (FAPESP), Brazil for their financial support of this work (grant numbers 2013/08293-7, 2020/07391-9 and 2022/06811-0).

Appendix A. Sensitivities for the equivalent piezoelectric material properties and geometry projection method

As in Section 4.5, the geometric design variables of the qth PSA $\boldsymbol{x}_{0_q}$, $\boldsymbol{x}_{\mathrm{f}_q}$ and d_q are represented by x_q. The notation specifying the mechanical $_{\mathrm{uu}}$, piezoelectric $_{\phi\mathrm{u}}$ and dielectric $_{\phi\phi}$ submatrices, SIMP exponents (w_{a}, w_{sv}, w_{cd}) and softargmax values (σ_{iq}) is also omitted. The derivatives of the $\boldsymbol{K}_{\mathrm{A}_{iq}}$ matrices of Eq. (28) with respect to x_q and α_q can be calculated, respectively, as

$$\begin{aligned}\frac{\partial \boldsymbol{K}_{\mathrm{A}_{iq}}}{\partial x_q} = {} & \frac{\partial \rho_{\mathrm{v}_{iq}}}{\partial x_q}\boldsymbol{K}_{\mathrm{V}} + w_{\mathrm{a}}\alpha_q^{w_{\mathrm{a}}}\left[\rho_{\mathrm{e}_{iq}}^{w_{\mathrm{a}}-1}\frac{\partial \rho_{\mathrm{e}_{iq}}}{\partial x_q}\left(\boldsymbol{K}_{\mathrm{E}_{iq}} - \boldsymbol{K}_{\mathrm{V}}\right) + \rho_{\mathrm{p}_{iq}}^{w_{\mathrm{a}}-1}\frac{\partial \rho_{\mathrm{p}_{iq}}}{\partial x_q}\left(\boldsymbol{K}_{\mathrm{P}_{iq}} - \boldsymbol{K}_{\mathrm{E}_{iq}}\right)\right] \\ & + \alpha_q^{w_{\mathrm{a}}}\left[\left(\rho_{\mathrm{e}_{iq}}^{w_{\mathrm{a}}} - \rho_{\mathrm{p}_{iq}}^{w_{\mathrm{a}}}\right)\frac{\partial \boldsymbol{K}_{\mathrm{E}_{iq}}}{\partial x_q} + \rho_{\mathrm{p}_{iq}}^{w_{\mathrm{a}}}\frac{\partial \boldsymbol{K}_{\mathrm{P}_{iq}}}{\partial x_q}\right]\end{aligned} \tag{63}$$

$$\frac{\partial \boldsymbol{K}_{\mathrm{A}_{iq}}}{\partial \alpha_q} = w_{\mathrm{a}} \alpha_q^{w_{\mathrm{a}}-1} \left[\rho_{\mathrm{e}_{iq}}^{w_{\mathrm{a}}} \left(\boldsymbol{K}_{\mathrm{E}_{iq}} - \boldsymbol{K}_{\mathrm{V}} \right) + \rho_{\mathrm{p}_{iq}}^{w_{\mathrm{a}}} \left(\boldsymbol{K}_{\mathrm{P}_{iq}} - \boldsymbol{K}_{\mathrm{E}_{iq}} \right) \right] \tag{64}$$

The derivatives of the submatrices of the equivalent piezoelectric material $\boldsymbol{K}_{\mathrm{P}_{iq}}$ and the electrode material $\boldsymbol{K}_{\mathrm{E}_{iq}}$ matrices with respect to x_q use Eq. (14). Omitting the subscripts P and E for ease of notation, their derivatives can be written once as

$$\begin{aligned}
\frac{\partial \boldsymbol{K}_{\mathrm{uu}_i}}{\partial x_q} &= \int_{\Omega_i} \boldsymbol{B}_{\mathrm{u}}^{\top} \frac{\partial \boldsymbol{c}^{\mathrm{E}}}{\partial x_q} \boldsymbol{B}_{\mathrm{u}} \, \mathrm{d}\,\Omega \\
\frac{\partial \boldsymbol{K}_{\phi\mathrm{u}_i}}{\partial x_q} &= \int_{\Omega_i} \boldsymbol{B}_{\phi}^{\top} \frac{\partial \boldsymbol{e}}{\partial x_q} \boldsymbol{B}_{\mathrm{u}} \, \mathrm{d}\,\Omega \\
\frac{\partial \boldsymbol{K}_{\phi\phi_i}}{\partial x_q} &= \int_{\Omega_i} \boldsymbol{B}_{\phi}^{\top} \frac{\partial \boldsymbol{\varepsilon}^{\mathrm{S}}}{\partial x_q} \boldsymbol{B}_{\phi} \, \mathrm{d}\,\Omega
\end{aligned} \tag{65}$$

where the properties are in the global coordinate system.

The submatrices of $\boldsymbol{K}_{\mathrm{P}_{iq}}$ use the equivalent piezoelectric material properties in the global coordinate system $\boldsymbol{c}_{\mathrm{p}}^{\mathrm{E}}$, $\boldsymbol{e}_{\mathrm{p}}$ and $\boldsymbol{\varepsilon}_{\mathrm{p}}^{\mathrm{S}}$, and their derivatives with respect to x_q are, from Eq. (25):

$$\frac{\partial \boldsymbol{c}_{\mathrm{p}}^{\mathrm{E}}}{\partial x_q} = \frac{\partial \boldsymbol{T}_{\mathrm{a}_q}^{\top}}{\partial x_q} \boldsymbol{c}_{\mathrm{p}}^{\mathrm{E}\prime} \boldsymbol{T}_{\mathrm{a}_q} + \boldsymbol{T}_{\mathrm{a}_q}^{\top} \boldsymbol{c}_{\mathrm{p}}^{\mathrm{E}\prime} \frac{\partial \boldsymbol{T}_{\mathrm{a}_q}}{\partial x_q} \tag{66}$$

$$\frac{\partial \boldsymbol{e}_{\mathrm{p}_q}}{\partial x_q} = \frac{\partial \boldsymbol{R}_{\mathrm{a}_q}^{\top}}{\partial x_q} \boldsymbol{e}'_{\mathrm{p}_q} \boldsymbol{T}_{\mathrm{a}_q} + \boldsymbol{R}_{\mathrm{a}_q}^{\top} \frac{\partial \boldsymbol{e}'_{\mathrm{p}_q}}{\partial x_q} \boldsymbol{T}_{\mathrm{a}_q} + \boldsymbol{R}_{\mathrm{a}_q}^{\top} \boldsymbol{e}'_{\mathrm{p}_q} \frac{\partial \boldsymbol{T}_{\mathrm{a}_q}}{\partial x_q} \tag{67}$$

$$\frac{\partial \boldsymbol{\varepsilon}_{\mathrm{p}_q}^{\mathrm{S}}}{\partial x_q} = \frac{\partial \boldsymbol{R}_{\mathrm{a}_q}^{\top}}{\partial x_q} \boldsymbol{\varepsilon}_{\mathrm{p}_q}^{\mathrm{S}\prime} \boldsymbol{R}_{\mathrm{a}_q} + \boldsymbol{R}_{\mathrm{a}_q}^{\top} \frac{\partial \boldsymbol{\varepsilon}_{\mathrm{p}_q}^{\mathrm{S}\prime}}{\partial x_q} \boldsymbol{R}_{\mathrm{a}_q} + \boldsymbol{R}_{\mathrm{a}_q}^{\top} \boldsymbol{\varepsilon}_{\mathrm{p}_q}^{\mathrm{S}\prime} \frac{\partial \boldsymbol{R}_{\mathrm{a}_q}}{\partial x_q} \tag{68}$$

Similarly, the submatrices of $\boldsymbol{K}_{\mathrm{E}_{iq}}$ use the electrode material properties in the global coordinate system $\boldsymbol{c}_{\mathrm{e}}^{\mathrm{E}}$, $\boldsymbol{e}_{\mathrm{e}}$ and $\boldsymbol{\varepsilon}_{\mathrm{e}}^{\mathrm{S}}$, and their derivatives with respect to x_q are, also from Eq. (25):

$$\frac{\partial \boldsymbol{c}_{\mathrm{e}}^{\mathrm{E}}}{\partial x_q} = \frac{\partial \boldsymbol{T}_{\mathrm{a}_q}^{\top}}{\partial x_q} \boldsymbol{c}_{\mathrm{e}}^{\mathrm{E}\prime} \boldsymbol{T}_{\mathrm{a}_q} + \boldsymbol{T}_{\mathrm{a}_q}^{\top} \boldsymbol{c}_{\mathrm{e}}^{\mathrm{E}\prime} \frac{\partial \boldsymbol{T}_{\mathrm{a}_q}}{\partial x_q} \tag{69}$$

$$\frac{\partial \boldsymbol{e}_{\mathrm{e}_q}}{\partial x_q} = \frac{\partial \boldsymbol{R}_{\mathrm{a}_q}^{\top}}{\partial x_q} \boldsymbol{e}'_{\mathrm{e}} \boldsymbol{T}_{\mathrm{a}_q} + \boldsymbol{R}_{\mathrm{a}_q}^{\top} \boldsymbol{e}'_{\mathrm{e}} \frac{\partial \boldsymbol{T}_{\mathrm{a}_q}}{\partial x_q} \tag{70}$$

$$\frac{\partial \boldsymbol{\varepsilon}_{\mathrm{e}_q}^{\mathrm{S}}}{\partial x_q} = \frac{\partial \boldsymbol{R}_{\mathrm{a}_q}^{\top}}{\partial x_q} \boldsymbol{\varepsilon}_{\mathrm{e}}^{\mathrm{S}\prime} \boldsymbol{R}_{\mathrm{a}_q} + \boldsymbol{R}_{\mathrm{a}_q}^{\top} \boldsymbol{\varepsilon}_{\mathrm{e}}^{\mathrm{S}\prime} \frac{\partial \boldsymbol{R}_{\mathrm{a}_q}}{\partial x_q} \tag{71}$$

The derivatives of the equivalent piezoelectric matrix and of the dielectric permittivity matrix are matrices of zeros, except for the positions where there are e_{31}, e_{33} and $\varepsilon_{33}^{\mathrm{S}}$. From Eq. (11), Section 2.1, the derivatives are

$$\begin{aligned}
\frac{\partial e'_{31_{\mathrm{PSA}}}}{\partial x_q} &= \frac{\partial n}{\partial x_q} e'_{31} = \frac{e'_{31}}{t_{\mathrm{d}}} \frac{\partial \|\boldsymbol{a}_q\|}{\partial x_q} = \frac{e'_{31}}{t_{\mathrm{d}}} \frac{\partial \boldsymbol{a}_q}{\partial x_q} \frac{\boldsymbol{a}_q}{\|\boldsymbol{a}_q\|} \\
\frac{\partial e'_{33_{\mathrm{PSA}}}}{\partial x_q} &= \frac{\partial n}{\partial x_q} e'_{33} = \frac{e'_{33}}{t_{\mathrm{d}}} \frac{\partial \|\boldsymbol{a}_q\|}{\partial x_q} = \frac{e'_{33}}{t_{\mathrm{d}}} \frac{\partial \boldsymbol{a}_q}{\partial x_q} \frac{\boldsymbol{a}_q}{\|\boldsymbol{a}_q\|} \\
\frac{\partial \varepsilon^{\mathrm{S}\prime}_{33_{\mathrm{PSA}}}}{\partial x_q} &= \frac{\partial n^2}{\partial x_q} \varepsilon_{33}^{\mathrm{S}\prime} = 2n \frac{\varepsilon_{33}^{\mathrm{S}\prime}}{t_{\mathrm{d}}} \frac{\partial \|\boldsymbol{a}_q\|}{\partial x_q} = 2n \frac{\varepsilon_{33}^{\mathrm{S}\prime}}{t_{\mathrm{d}}} \frac{\partial \boldsymbol{a}_q}{\partial x_q} \frac{\boldsymbol{a}_q}{\|\boldsymbol{a}_q\|}
\end{aligned} \tag{72}$$

From Eq. (16), the derivatives of $\boldsymbol{a}_q$ with respect to the geometric design variables are

$$\frac{\partial \boldsymbol{a}_q}{\partial \boldsymbol{x}_{0_q}} = -\mathbf{I} \qquad \frac{\partial \boldsymbol{a}_q}{\partial \boldsymbol{x}_{\mathrm{f}_q}} = \mathbf{I} \qquad \frac{\partial \boldsymbol{a}_q}{\partial d_q} = \mathbf{0} \tag{73}$$

where $\mathbf{I}$ is an identity matrix of size 2×2 in 2D or 3×3 in 3D.

The derivatives of the rotation matrices $\boldsymbol{R}_{\mathrm{a}_q}$ and $\boldsymbol{T}_{\mathrm{a}_q}$ of the qth PSA with respect to d_q are equal to 0. Since their derivatives with respect to $\boldsymbol{x}_{0_q}$ and $\boldsymbol{x}_{\mathrm{f}_q}$ yield third-order tensors, they are given in index notation in terms of the kth component of vectors $\boldsymbol{x}_{0_q}$ and $\boldsymbol{x}_{\mathrm{f}_q}$. Additionally, two auxiliary vectors are used: $\boldsymbol{e}_1 = \{1, 0\}^{\top}$ and $\boldsymbol{e}_2 = \{0, 1\}^{\top}$.

$$\frac{\partial \boldsymbol{R}_{\mathrm{a}_q}}{\partial x_{0_{q_k}}} = \frac{a_{q_k}}{\|\boldsymbol{a}_q\|^2} \begin{bmatrix} a_{q_z} & -a_{q_x} \\ a_{q_x} & a_{q_z} \end{bmatrix} + \frac{1}{\|\boldsymbol{a}_q\|} \begin{bmatrix} -e_{2_k} & e_{1_k} \\ -e_{1_k} & -e_{2_k} \end{bmatrix} \tag{74}$$

$$\frac{\partial \boldsymbol{R}_{\mathrm{a}_q}}{\partial x_{f_{q_k}}} = -\frac{a_{q_k}}{\|\boldsymbol{a}_q\|^2} \begin{bmatrix} a_{q_z} & -a_{q_x} \\ a_{q_x} & a_{q_z} \end{bmatrix} + \frac{1}{\|\boldsymbol{a}_q\|} \begin{bmatrix} e_{2_k} & -e_{1_k} \\ e_{1_k} & e_{2_k} \end{bmatrix} \tag{75}$$

$$\frac{\partial \boldsymbol{T}_{\mathrm{a}_q}}{\partial x_{0_{q_k}}} = \frac{2a_{q_k}}{\|\boldsymbol{a}_q\|^4}\begin{bmatrix} a_{q_z}^2 & a_{q_x}^2 & -a_{q_x}a_{q_z} \\ a_{q_x}^2 & a_{q_z}^2 & a_{q_x}a_{q_z} \\ 2a_{q_x}a_{q_z} & -2a_{q_x}a_{q_z} & a_{q_z}^2 - a_{q_x}^2 \end{bmatrix} + \frac{1}{\|\boldsymbol{a}_q\|^2}\begin{bmatrix} -2a_{q_z}e_{2_k} & -2a_{q_x}e_{1_k} & a_{q_z}e_{1_k} + a_{q_x}e_{2_k} \\ -2a_{q_x}e_{1_k} & -2a_{q_z}e_{2_k} & -a_{q_z}e_{1_k} - a_{q_x}e_{2_k} \\ -2a_{q_z}e_{1_k} - 2a_{q_x}e_{2_k} & 2a_{q_z}e_{1_k} + 2a_{q_x}e_{2_k} & -2a_{q_z}e_{2_k} + 2a_{q_x}e_{1_k} \end{bmatrix} \tag{76}$$

$$\frac{\partial \boldsymbol{T}_{\mathrm{a}_q}}{\partial x_{\mathrm{f}_{q_k}}} = -\frac{2a_{q_k}}{\|\boldsymbol{a}_q\|^4}\begin{bmatrix} a_{q_z}^2 & a_{q_x}^2 & -a_{q_x}a_{q_z} \\ a_{q_x}^2 & a_{q_z}^2 & a_{q_x}a_{q_z} \\ 2a_{q_x}a_{q_z} & -2a_{q_x}a_{q_z} & a_{q_z}^2 - a_{q_x}^2 \end{bmatrix} + \frac{1}{\|\boldsymbol{a}_q\|^2}\begin{bmatrix} 2a_{q_z}e_{2_k} & 2a_{q_x}e_{1_k} & -a_{q_z}e_{1_k} - a_{q_x}e_{2_k} \\ 2a_{q_x}e_{1_k} & 2a_{q_z}e_{2_k} & a_{q_z}e_{1_k} + a_{q_x}e_{2_k} \\ 2a_{q_z}e_{1_k} + 2a_{q_x}e_{2_k} & -2a_{q_z}e_{1_k} - 2a_{q_x}e_{2_k} & 2a_{q_z}e_{2_k} - 2a_{q_x}e_{1_k} \end{bmatrix} \tag{77}$$

For the derivatives of $\rho_{\mathrm{v}_{iq}}$, $\rho_{\mathrm{e}_{iq}}$ and $\rho_{\mathrm{p}_{iq}}$ with respect to the geometric variables x_q, firstly we have to define the derivatives of the offset geometric variables with respect to the original ones using Eq. (22):

$$\begin{aligned} \frac{\partial \boldsymbol{x}_{0_q}^{\mathrm{os}}}{\partial \boldsymbol{x}_{0_q}} &= \frac{\partial \boldsymbol{x}_{\mathrm{f}_q}^{\mathrm{os}}}{\partial \boldsymbol{x}_{\mathrm{f}_q}} = \mathbf{I} + \frac{l'}{2}\left(\frac{1}{\|\boldsymbol{a}_q\|}\mathbf{I} - \frac{\boldsymbol{a}_q \otimes \boldsymbol{a}_q}{\|\boldsymbol{a}_q\|^3}\right) \\ \frac{\partial \boldsymbol{x}_{0_q}^{\mathrm{os}}}{\partial \boldsymbol{x}_{\mathrm{f}_q}} &= \frac{\partial \boldsymbol{x}_{\mathrm{f}_q}^{\mathrm{os}}}{\partial \boldsymbol{x}_{0_q}} = -\frac{l'}{2}\left(\frac{1}{\|\boldsymbol{a}_q\|}\mathbf{I} - \frac{\boldsymbol{a}_q \otimes \boldsymbol{a}_q}{\|\boldsymbol{a}_q\|^3}\right) \\ \frac{\partial d_q^{\mathrm{os}}}{\partial d_q} &= 1 \end{aligned} \tag{78}$$

$$\frac{\partial \boldsymbol{x}_{0_q}^{\mathrm{os}}}{\partial d_q} = \frac{\partial \boldsymbol{x}_{\mathrm{f}_q}^{\mathrm{os}}}{\partial d_q} = \frac{\partial d_q^{\mathrm{os}}}{\partial \boldsymbol{x}_{0_q}} = \frac{\partial d_q^{\mathrm{os}}}{\partial \boldsymbol{x}_{\mathrm{f}_q}} = \mathbf{0} \tag{79}$$

where $\otimes$ means outer product.

Then, using $\rho_i(x_q)$ from Eq. (20), the derivatives of $\rho_{\mathrm{v}_{iq}}$, $\rho_{\mathrm{e}_{iq}}$ and $\rho_{\mathrm{p}_{iq}}$ with respect to $\boldsymbol{x}_{0_q}$ can be found using Eqs. (21)–(24):

$$\begin{aligned} \frac{\partial \rho_{\mathrm{p}_{iq}}}{\partial \boldsymbol{x}_{0_q}} &= \frac{\partial \rho_i(\boldsymbol{x}_{0_q}, \boldsymbol{x}_{\mathrm{f}_q}, d_q)}{\partial \boldsymbol{x}_{0_q}} \\ \frac{\partial \rho_{\mathrm{e}_{iq}}}{\partial \boldsymbol{x}_{0_q}} &= \frac{\partial \rho_i(\boldsymbol{x}_{0_q}^{\mathrm{os}}, \boldsymbol{x}_{\mathrm{f}_q}^{\mathrm{os}}, d_q)}{\partial \boldsymbol{x}_{0_q}^{\mathrm{os}}}\frac{\partial \boldsymbol{x}_{0_q}^{\mathrm{os}}}{\partial \boldsymbol{x}_{0_q}} + \frac{\partial \rho_i(\boldsymbol{x}_{0_q}^{\mathrm{os}}, \boldsymbol{x}_{\mathrm{f}_q}^{\mathrm{os}}, d_q)}{\partial \boldsymbol{x}_{\mathrm{f}_q}^{\mathrm{os}}}\frac{\partial \boldsymbol{x}_{\mathrm{f}_q}^{\mathrm{os}}}{\partial \boldsymbol{x}_{0_q}} \\ \frac{\partial \rho_{\mathrm{v}_{iq}}}{\partial \boldsymbol{x}_{0_q}} &= \frac{\partial \rho_i(\boldsymbol{x}_{0_q}^{\mathrm{os}}, \boldsymbol{x}_{\mathrm{f}_q}^{\mathrm{os}}, d_q^{\mathrm{os}})}{\partial \boldsymbol{x}_{0_q}^{\mathrm{os}}}\frac{\partial \boldsymbol{x}_{0_q}^{\mathrm{os}}}{\partial \boldsymbol{x}_{0_q}} + \frac{\partial \rho_i(\boldsymbol{x}_{0_q}^{\mathrm{os}}, \boldsymbol{x}_{\mathrm{f}_q}^{\mathrm{os}}, d_q^{\mathrm{os}})}{\partial \boldsymbol{x}_{\mathrm{f}_q}^{\mathrm{os}}}\frac{\partial \boldsymbol{x}_{\mathrm{f}_q}^{\mathrm{os}}}{\partial \boldsymbol{x}_{0_q}} \end{aligned} \tag{80}$$

Similarly, their derivatives with respect to $\boldsymbol{x}_{\mathrm{f}_q}$ are

$$\begin{aligned} \frac{\partial \rho_{\mathrm{p}_{iq}}}{\partial \boldsymbol{x}_{\mathrm{f}_q}} &= \frac{\partial \rho_i(\boldsymbol{x}_{0_q}, \boldsymbol{x}_{\mathrm{f}_q}, d_q)}{\partial \boldsymbol{x}_{\mathrm{f}_q}} \\ \frac{\partial \rho_{\mathrm{e}_{iq}}}{\partial \boldsymbol{x}_{\mathrm{f}_q}} &= \frac{\partial \rho_i(\boldsymbol{x}_{0_q}^{\mathrm{os}}, \boldsymbol{x}_{\mathrm{f}_q}^{\mathrm{os}}, d_q)}{\partial \boldsymbol{x}_{0_q}^{\mathrm{os}}}\frac{\partial \boldsymbol{x}_{0_q}^{\mathrm{os}}}{\partial \boldsymbol{x}_{\mathrm{f}_q}} + \frac{\partial \rho_i(\boldsymbol{x}_{0_q}^{\mathrm{os}}, \boldsymbol{x}_{\mathrm{f}_q}^{\mathrm{os}}, d_q)}{\partial \boldsymbol{x}_{\mathrm{f}_q}^{\mathrm{os}}}\frac{\partial \boldsymbol{x}_{\mathrm{f}_q}^{\mathrm{os}}}{\partial \boldsymbol{x}_{\mathrm{f}_q}} \\ \frac{\partial \rho_{\mathrm{v}_{iq}}}{\partial \boldsymbol{x}_{\mathrm{f}_q}} &= \frac{\partial \rho_i(\boldsymbol{x}_{0_q}^{\mathrm{os}}, \boldsymbol{x}_{\mathrm{f}_q}^{\mathrm{os}}, d_q^{\mathrm{os}})}{\partial \boldsymbol{x}_{0_q}^{\mathrm{os}}}\frac{\partial \boldsymbol{x}_{0_q}^{\mathrm{os}}}{\partial \boldsymbol{x}_{\mathrm{f}_q}} + \frac{\partial \rho_i(\boldsymbol{x}_{0_q}^{\mathrm{os}}, \boldsymbol{x}_{\mathrm{f}_q}^{\mathrm{os}}, d_q^{\mathrm{os}})}{\partial \boldsymbol{x}_{\mathrm{f}_q}^{\mathrm{os}}}\frac{\partial \boldsymbol{x}_{\mathrm{f}_q}^{\mathrm{os}}}{\partial \boldsymbol{x}_{\mathrm{f}_q}} \end{aligned} \tag{81}$$

And their derivatives with respect to d_q are

$$\begin{aligned} \frac{\partial \rho_{\mathrm{p}_{iq}}}{\partial d_q} &= \frac{\partial \rho_i(\boldsymbol{x}_{0_q}, \boldsymbol{x}_{\mathrm{f}_q}, d_q)}{\partial d_q} \\ \frac{\partial \rho_{\mathrm{e}_{iq}}}{\partial d_q} &= \frac{\partial \rho_i(\boldsymbol{x}_{0_q}^{\mathrm{os}}, \boldsymbol{x}_{\mathrm{f}_q}^{\mathrm{os}}, d_q)}{\partial d_q} \\ \frac{\partial \rho_{\mathrm{v}_{iq}}}{\partial d_q} &= \frac{\partial \rho_i(\boldsymbol{x}_{0_q}^{\mathrm{os}}, \boldsymbol{x}_{\mathrm{f}_q}^{\mathrm{os}}, d_q^{\mathrm{os}})}{\partial d_q^{\mathrm{os}}} \end{aligned} \tag{82}$$

Writing $\rho_i(x_q)$ from Eq. (20) as a function of any geometric parameter x_q (including the offset ones), its derivative with respect to x_q is:

$$\frac{\partial \rho_i(x_q)}{\partial x_q} = \sum_j^N w_j \frac{\partial \tilde{H}_{ij}(x_q)}{\partial x_q} \tag{83}$$

The derivative of the piecewise smooth Heaviside $\tilde{H}(x)$ from Eq. (18) is:

$$\frac{\partial \tilde{H}(x)}{\partial x} = \begin{cases} 6\dfrac{x^2}{w^3} - \dfrac{3}{2w}, & \text{if } |x| \le \frac{w}{2} \\ 0, & \text{otherwise.} \end{cases} \tag{84}$$

Finally, the derivatives of the rectangular signed-distance function $\varphi(x_q, \boldsymbol{p})$ from Eq. (15) with respect to the geometric variables of the qth PSA can be written as shown in the following equations. Here the subscript "q" referring to the qth PSA was omitted for simplicity.

$$\frac{\partial \varphi}{\partial \boldsymbol{x}_0} = \begin{cases} \dfrac{\boldsymbol{g}+\boldsymbol{a}}{\|\boldsymbol{a}\|} & \text{if } \|\boldsymbol{g}\| \le \frac{d}{2} \text{ and } \boldsymbol{b}'\cdot\boldsymbol{a} < -\frac{\sqrt{2}}{2}\|\boldsymbol{b}'\|\|\boldsymbol{a}\| \\ -\dfrac{\boldsymbol{g}}{\|\boldsymbol{a}\|} & \text{if } \|\boldsymbol{g}\| \le \frac{d}{2} \text{ and } \boldsymbol{e}'\cdot\boldsymbol{a} > \frac{\sqrt{2}}{2}\|\boldsymbol{e}'\|\|\boldsymbol{a}\| \\ -\dfrac{1}{\|\boldsymbol{b}''\|}\left(\boldsymbol{b} + \dfrac{d}{2}\dfrac{\boldsymbol{e}\cdot\boldsymbol{a}}{\boldsymbol{a}\cdot\boldsymbol{a}}\dfrac{\boldsymbol{g}}{\|\boldsymbol{g}\|}\right) & \text{if } \|\boldsymbol{g}\| > \frac{d}{2} \text{ and } \boldsymbol{b}\cdot\boldsymbol{a} < 0 \\ -\dfrac{1}{\|\boldsymbol{e}''\|}\dfrac{d}{2}\dfrac{\boldsymbol{e}\cdot\boldsymbol{a}}{\boldsymbol{a}\cdot\boldsymbol{a}}\dfrac{\boldsymbol{g}}{\|\boldsymbol{g}\|} & \text{if } \|\boldsymbol{g}\| > \frac{d}{2} \text{ and } \boldsymbol{e}\cdot\boldsymbol{a} > 0 \\ \dfrac{\boldsymbol{e}\cdot\boldsymbol{a}}{\boldsymbol{a}\cdot\boldsymbol{a}}\dfrac{\boldsymbol{g}}{\|\boldsymbol{g}\|} & \text{otherwise} \end{cases} \tag{85}$$

$$\frac{\partial \varphi}{\partial \boldsymbol{x}_\mathrm{f}} = \begin{cases} -\dfrac{\boldsymbol{g}}{\|\boldsymbol{a}\|} & \text{if } \|\boldsymbol{g}\| \le \frac{d}{2} \text{ and } \boldsymbol{b}'\cdot\boldsymbol{a} < -\frac{\sqrt{2}}{2}\|\boldsymbol{b}'\|\|\boldsymbol{a}\| \\ \dfrac{\boldsymbol{g}-\boldsymbol{a}}{\|\boldsymbol{a}\|} & \text{if } \|\boldsymbol{g}\| \le \frac{d}{2} \text{ and } \boldsymbol{e}'\cdot\boldsymbol{a} > \frac{\sqrt{2}}{2}\|\boldsymbol{e}'\|\|\boldsymbol{a}\| \\ \dfrac{1}{\|\boldsymbol{b}''\|}\dfrac{d}{2}\dfrac{\boldsymbol{b}\cdot\boldsymbol{a}}{\boldsymbol{a}\cdot\boldsymbol{a}}\dfrac{\boldsymbol{g}}{\|\boldsymbol{g}\|} & \text{if } \|\boldsymbol{g}\| > \frac{d}{2} \text{ and } \boldsymbol{b}\cdot\boldsymbol{a} < 0 \\ \dfrac{1}{\|\boldsymbol{e}''\|}\left(\dfrac{d}{2}\dfrac{\boldsymbol{b}\cdot\boldsymbol{a}}{\boldsymbol{a}\cdot\boldsymbol{a}}\dfrac{\boldsymbol{g}}{\|\boldsymbol{g}\|} - \boldsymbol{e}\right) & \text{if } \|\boldsymbol{g}\| > \frac{d}{2} \text{ and } \boldsymbol{e}\cdot\boldsymbol{a} > 0 \\ -\dfrac{\boldsymbol{b}\cdot\boldsymbol{a}}{\boldsymbol{a}\cdot\boldsymbol{a}}\dfrac{\boldsymbol{g}}{\|\boldsymbol{g}\|} & \text{otherwise} \end{cases} \tag{86}$$

$$\frac{\partial \varphi}{\partial d} = \begin{cases} 0 & \text{if } \|\boldsymbol{g}\| \le \frac{d}{2} \text{ and } \boldsymbol{b}'\cdot\boldsymbol{a} < -\frac{\sqrt{2}}{2}\|\boldsymbol{b}'\|\|\boldsymbol{a}\| \\ 0 & \text{if } \|\boldsymbol{g}\| \le \frac{d}{2} \text{ and } \boldsymbol{e}'\cdot\boldsymbol{a} > \frac{\sqrt{2}}{2}\|\boldsymbol{e}'\|\|\boldsymbol{a}\| \\ \dfrac{1}{2\|\boldsymbol{b}''\|}\left(\dfrac{d}{2} - \|\boldsymbol{g}\|\right) & \text{if } \|\boldsymbol{g}\| > \frac{d}{2} \text{ and } \boldsymbol{b}\cdot\boldsymbol{a} < 0 \\ \dfrac{1}{2\|\boldsymbol{e}''\|}\left(\dfrac{d}{2} - \|\boldsymbol{g}\|\right) & \text{if } \|\boldsymbol{g}\| > \frac{d}{2} \text{ and } \boldsymbol{e}\cdot\boldsymbol{a} > 0 \\ -\dfrac{1}{2} & \text{otherwise} \end{cases} \tag{87}$$

Note that $\frac{\partial \varphi(x_q,\boldsymbol{p})}{\partial x_q}$ does not have to be calculated at every sampling point, but only where the derivative of $\tilde{H}\left(\varphi\left(\boldsymbol{x}_q, \boldsymbol{p}\right)\right)$ is non-zero.

Appendix B. Properties of the electrode and piezoelectric materials.

The piezoelectric material of each disc within the PSA is PZT-5. Its elastic stiffness, piezoelectric and dielectric permittivity matrices are shown in Eqs. (88), (89) and (90), respectively, in the local coordinate system.

$$\boldsymbol{c}_\mathrm{p}^{\mathrm{E}\prime} = \begin{bmatrix} 121 & 75.4 & 75.2 & & & \\ 75.4 & 121 & 75.2 & & & \\ 75.2 & 75.2 & 111 & & & \\ & & & 21 & & \\ & & & & 21 & \\ & & & & & 23 \end{bmatrix} \text{GPa} \tag{88}$$

$$\boldsymbol{e}_\mathrm{p}' = \begin{bmatrix} & & & & 12.3 & \\ & & & 12.3 & & \\ -5.4 & -5.4 & 15.8 & & & \end{bmatrix} \frac{\mathrm{C}}{\mathrm{m}^2} \tag{89}$$

$$\boldsymbol{\epsilon}_{\mathrm{p}}^{\mathrm{S}\prime} = \begin{bmatrix} 14.61 & & \\ & 14.61 & \\ & & 15.05 \end{bmatrix} 10^{-9}\,\frac{\mathrm{F}}{\mathrm{m}} \tag{90}$$

The material of the electrode has the elastic stiffness matrix shown in Eq. (91). It has no piezoelectricity and an isotropic absolute permittivity of $8.9073 \cdot 10^{-3}\ \frac{\mathrm{F}}{\mathrm{m}}$, i.e. the same as of the conductive material.

$$\boldsymbol{c}_{\mathrm{e}}^{\mathrm{E}\prime} = \begin{bmatrix} 262.09 & 107.05 & 107.05 & & & \\ 107.05 & 262.09 & 107.05 & & & \\ 107.05 & 107.05 & 262.09 \cdot 10^{9} & & & \\ & & & 7.7519 \cdot 10^{7} & & \\ & & & & 7.7519 \cdot 10^{7} & \\ & & & & & 7.7519 \cdot 10^{7} \end{bmatrix} \mathrm{Pa} \tag{91}$$

References

[1] H. Janocha (Ed.), Adaptronics and Smart Structures, second ed., Springer, Berlin, 2007.
[2] J. Sun, Q. Guan, Y. Liu, J. Leng, Morphing aircraft based on smart materials and structures: A state-of-the-art review, J. Intell. Mater. Syst. Struct. 27 (17) (2016) 2289–2312, http://dx.doi.org/10.1177/1045389x16629569.
[3] S. Sony, S. Laventure, A. Sadhu, A literature review of next-generation smart sensing technology in structural health monitoring, Struct. Control Health Monit. 26 (3) (2019) e2321, http://dx.doi.org/10.1002/stc.2321.
[4] M. Aflori, Smart nanomaterials for biomedical applications—A review, Nanomaterials 11 (2) (2021) 396, http://dx.doi.org/10.3390/nano11020396.
[5] J.M. Sinapius, Adaptronics – Smart Structures and Materials, Springer Berlin Heidelberg, 2021, http://dx.doi.org/10.1007/978-3-662-61399-3.
[6] M.P. Bendsoe, O. Sigmund, Topology Optimization: Theory, Methods, and Applications, Springer-Verlag, 2013.
[7] M.P. Bendsøe, O. Sigmund, Material interpolation schemes in topology optimization, Arch. Appl. Mech. (Ingen. Arch.) 69 (9–10) (1999) 635–654, http://dx.doi.org/10.1007/s004190050248.
[8] O. Sigmund, S. Torquato, Design of materials with extreme thermal expansion using a three-phase topology optimization method, J. Mech. Phys. Solids 45 (6) (1997) 1037–1067, http://dx.doi.org/10.1016/s0022-5096(96)00114-7.
[9] O. Sigmund, Design of multiphysics actuators using topology optimization – Part II: Two-material structures, Comput. Methods Appl. Mech. Engrg. 190 (49) (2001) 6605–6627, http://dx.doi.org/10.1016/S0045-7825(01)00252-3.
[10] T. Gao, W. Zhang, A mass constraint formulation for structural topology optimization with multiphase materials, Internat. J. Numer. Methods Engrg. 88 (8) (2011) 774–796, http://dx.doi.org/10.1002/nme.3197.
[11] C.F. Hvejsel, E. Lund, Material interpolation schemes for unified topology and multi-material optimization, Struct. Multidiscip. Optim. 43 (6) (2011) 811–825, http://dx.doi.org/10.1007/s00158-011-0625-z.
[12] O. Sigmund, K. Maute, Topology optimization approaches, Struct. Multidiscip. Optim. 48 (6) (2013) 1031–1055, http://dx.doi.org/10.1007/s00158-013-0978-6.
[13] N.P. van Dijk, K. Maute, M. Langelaar, F. van Keulen, Level-set methods for structural topology optimization: A review, Struct. Multidiscip. Optim. 48 (3) (2013) 437–472, http://dx.doi.org/10.1007/s00158-013-0912-y.
[14] M.Y. Wang, X. Wang, "Color" level sets: a multi-phase method for structural topology optimization with multiple materials, Comput. Methods Appl. Mech. Engrg. 193 (6–8) (2004) 469–496, http://dx.doi.org/10.1016/j.cma.2003.10.008.
[15] M.Y. Wang, X. Wang, A level-set based variational method for design and optimization of heterogeneous objects, Comput. Aided Des. 37 (3) (2005) 321–337, http://dx.doi.org/10.1016/j.cad.2004.03.007.
[16] Y. Wang, Z. Luo, Z. Kang, N. Zhang, A multi-material level set-based topology and shape optimization method, Comput. Methods Appl. Mech. Engrg. 283 (2015) 1570–1586, http://dx.doi.org/10.1016/j.cma.2014.11.002.
[17] M. Kögl, E.C.N. Silva, Topology optimization of smart structures: Design of piezoelectric plate and shell actuators, Smart Mater. Struct. 14 (2) (2005) 387–399, http://dx.doi.org/10.1088/0964-1726/14/2/013.
[18] R.C. Carbonari, E.C.N. Silva, S. Nishiwaki, Optimum placement of piezoelectric material in piezoactuator design, Smart Mater. Struct. 16 (1) (2007) 207–220, http://dx.doi.org/10.1088/0964-1726/16/1/025.
[19] L.A. Motta Mello, C.Y. Kiyono, P.H. Nakasone, E.C. Nelli Silva, Design of quasi-static piezoelectric plate based transducers by using topology optimization, Smart Mater. Struct. 23 (2) (2014) 025035, http://dx.doi.org/10.1088/0964-1726/23/2/025035.
[20] X. Zhang, A. Takezawa, Z. Kang, Topology optimization of piezoelectric smart structures for minimum energy consumption under active control, Struct. Multidiscip. Optim. 58 (1) (2018) 185–199, http://dx.doi.org/10.1007/s00158-017-1886-y.
[21] Z. Luo, L. Tong, H. Ma, Shape and topology optimization for electrothermomechanical microactuators using level set methods, J. Comput. Phys. 228 (9) (2009) 3173–3181, http://dx.doi.org/10.1016/j.jcp.2009.01.010.
[22] Z. Luo, L. Tong, J. Luo, P. Wei, M.Y. Wang, Design of piezoelectric actuators using a multiphase level set method of piecewise constants, J. Comput. Phys. 228 (7) (2009) 2643–2659, http://dx.doi.org/10.1016/j.jcp.2008.12.019.
[23] E.M. de Souza, E.C.N. Silva, Topology optimization applied to the design of actuators driven by pressure loads, Struct. Multidiscip. Optim. 61 (5) (2020) 1763–1786, http://dx.doi.org/10.1007/s00158-019-02421-5.
[24] Z. Kang, K.A. James, Multiphysics design of programmable shape-memory alloy-based smart structures via topology optimization, Struct. Multidiscip. Optim. 65 (1) (2022) http://dx.doi.org/10.1007/s00158-021-03101-z.
[25] X. Gao, J. Yang, J. Wu, X. Xin, Z. Li, X. Yuan, X. Shen, S. Dong, Piezoelectric actuators and motors: Materials, designs, and applications, Adv. Mater. Technol. 5 (1) (2020) 1900716, http://dx.doi.org/10.1002/admt.201900716.
[26] J. Lai, L. Yu, L. Yuan, J. Liang, M. Ling, R. Wang, H. Zang, H. Li, B. Zhu, X. Zhang, An integrated modeling method for piezo-actuated compliant mechanisms, Sensors Actuators A 364 (2023) 114770, http://dx.doi.org/10.1016/j.sna.2023.114770.
[27] S. Mohith, A.R. Upadhya, K.P. Navin, S.M. Kulkarni, M. Rao, Recent trends in piezoelectric actuators for precision motion and their applications: a review, Smart Mater. Struct. 30 (1) (2021) 013002, http://dx.doi.org/10.1088/1361-665x/abc6b9.
[28] K. Uchino (Ed.), Advanced Piezoelectric Materials, second ed., in: Woodhead Publishing Series in Electronic and Optical Materials, Woodhead Publishing / Elsevier, Duxford, 2017.
[29] E.C.N. Silva, N. Kikuchi, Design of piezoelectric transducers using topology optimization, Smart Mater. Struct. 8 (3) (1999) 350–364, http://dx.doi.org/10.1088/0964-1726/8/3/307.
[30] E.C.N. Silva, S. Nishiwaki, N. Kikuchi, Design of piezocomposite materials and piezoelectric transducers using topology optimization—Part II, Arch. Comput. Methods Eng. 6 (3) (1999) 191–215, http://dx.doi.org/10.1007/bf02896423.

[31] P.H. Nakasone, E.C.N. Silva, Dynamic design of piezoelectric laminated sensors and actuators using topology optimization, J. Intell. Mater. Syst. Struct. 21 (16) (2010) 1627–1652, http://dx.doi.org/10.1177/1045389x10386130.
[32] C.Y. Kiyono, E.C.N. Silva, J.N. Reddy, Design of laminated piezocomposite shell transducers with arbitrary fiber orientation using topology optimization approach, Internat. J. Numer. Methods Engrg. 90 (12) (2012) 1452–1484, http://dx.doi.org/10.1002/nme.3371.
[33] Y. Wang, Z. Luo, X. Zhang, Z. Kang, Topological design of compliant smart structures with embedded movable actuators, Smart Mater. Struct. 23 (4) (2014) 045024, http://dx.doi.org/10.1088/0964-1726/23/4/045024.
[34] R. Amigo, S.M. Giusti, A.A. Novotny, E.C.N. Silva, J. Sokołowski, Optimum design of flextensional piezoelectric actuators into two spatial dimensions, SIAM J. Control Optim. 54 (2) (2016) 760–789, http://dx.doi.org/10.1137/151004860.
[35] C.Y. Kiyono, E.C.N. Silva, J.N. Reddy, Optimal design of laminated piezocomposite energy harvesting devices considering stress constraints, Internat. J. Numer. Methods Engrg. 105 (12) (2016) 883–914, http://dx.doi.org/10.1002/nme.4996.
[36] K. Yang, J. Zhu, M. Wu, W. Zhang, Integrated optimization of actuators and structural topology of piezoelectric composite structures for static shape control, Comput. Methods Appl. Mech. Engrg. 334 (2018) 440–469, http://dx.doi.org/10.1016/j.cma.2018.01.021.
[37] A. Homayouni-Amlashi, A. Mohand-Ousaid, M. Rakotondrabe, Topology optimization of 2DOF piezoelectric plate energy harvester under external in-plane force, J. Micro-Bio Robot. 16 (1) (2020) 65–77, http://dx.doi.org/10.1007/s12213-020-00129-0.
[38] B. Yang, C. Cheng, X. Wang, Z. Meng, A. Homayouni-Amlashi, Reliability-based topology optimization of piezoelectric smart structures with voltage uncertainty, J. Intell. Mater. Syst. Struct. 33 (15) (2022) 1975–1989, http://dx.doi.org/10.1177/1045389x211072197.
[39] R. Wang, X. Zhang, B. Zhu, F. Qu, B. Chen, J. Liang, Hybrid explicit–implicit topology optimization method for the integrated layout design of compliant mechanisms and actuators, Mech. Mach. Theory 171 (2022) 104750, http://dx.doi.org/10.1016/j.mechmachtheory.2022.104750.
[40] J. Hu, M. Wallin, M. Ristinmaa, Y. Liu, S. Liu, Integrated multi-material and multi-scale optimization of compliant structure with embedded movable piezoelectric actuators, Comput. Methods Appl. Mech. Engrg. 421 (2024) 116786, http://dx.doi.org/10.1016/j.cma.2024.116786.
[41] J.R. Banerjee, Review of the dynamic stiffness method for free-vibration analysis of beams, Transp. Saf. Environ. 1 (2) (2019) 106–116, http://dx.doi.org/10.1093/tse/tdz005.
[42] F. Wein, P.D. Dunning, J.A. Norato, A review on feature-mapping methods for structural optimization, Struct. Multidiscip. Optim. 62 (4) (2020) 1597–1638, http://dx.doi.org/10.1007/s00158-020-02649-6.
[43] J. Norato, B. Bell, D. Tortorelli, A geometry projection method for continuum-based topology optimization with discrete elements, Comput. Methods Appl. Mech. Engrg. 293 (2015) 306–327, http://dx.doi.org/10.1016/j.cma.2015.05.005.
[44] S.J. Rupitsch, Piezoelectric Sensors and Actuators, Springer Berlin Heidelberg, 2019, http://dx.doi.org/10.1007/978-3-662-57534-5.
[45] G.H. Yoon, O. Sigmund, A monolithic approach for topology optimization of electrostatically actuated devices, Comput. Methods Appl. Mech. Engrg. 197 (45–48) (2008) 4062–4075, http://dx.doi.org/10.1016/j.cma.2008.04.004.
[46] S. Chen, S. Gonella, W. Chen, W.K. Liu, A level set approach for optimal design of smart energy harvesters, Comput. Methods Appl. Mech. Engrg. 199 (37–40) (2010) 2532–2543, http://dx.doi.org/10.1016/j.cma.2010.04.008.
[47] M. He, X. Zhang, L. dos Santos Fernandez, A. Molter, L. Xia, T. Shi, Multi-material topology optimization of piezoelectric composite structures for energy harvesting, Compos. Struct. (2021) 113783, http://dx.doi.org/10.1016/j.compstruct.2021.113783.
[48] S.J. Rupitsch, Piezoelectric positioning systems and motors, in: Piezoelectric Sensors and Actuators, Springer Berlin Heidelberg, 2019, pp. 511–550, http://dx.doi.org/10.1007/978-3-662-57534-5_10.
[49] IEEE, IEEE standard on piezoelectricity, ANSI/IEEE Std 176-1987 (1988) http://dx.doi.org/10.1109/IEEESTD.1988.79638.
[50] R. Lerch, Simulation of piezoelectric devices by two- and three-dimensional finite elements, IEEE Trans. Ultrason. Ferroelectr. Freq. Control 37 (3) (1990) 233–247, http://dx.doi.org/10.1109/58.55314.
[51] B. Zheng, C.-J. Chang, H.C. Gea, Topology optimization of energy harvesting devices using piezoelectric materials, Struct. Multidiscip. Optim. 38 (1) (2008) 17–23, http://dx.doi.org/10.1007/s00158-008-0265-0.
[52] J.Y. Noh, G.H. Yoon, Topology optimization of piezoelectric energy harvesting devices considering static and harmonic dynamic loads, Adv. Eng. Softw. 53 (2012) 45–60, http://dx.doi.org/10.1016/j.advengsoft.2012.07.008.
[53] H. Smith, J.A. Norato, Topology optimization with discrete geometric components made of composite materials, Comput. Methods Appl. Mech. Engrg. 376 (2021) 113582, http://dx.doi.org/10.1016/j.cma.2020.113582.
[54] H. Smith, J. Norato, Topology optimization of structures made of fiber-reinforced plates, Struct. Multidiscip. Optim. 65 (2) (2022) http://dx.doi.org/10.1007/s00158-021-03164-y.
[55] Y. Zhou, W. Zhang, J. Zhu, Z. Xu, Feature-driven topology optimization method with signed distance function, Comput. Methods Appl. Mech. Engrg. 310 (2016) 1–32, http://dx.doi.org/10.1016/j.cma.2016.06.027.
[56] X. Wang, K. Long, V.-N. Hoang, P. Hu, An explicit optimization model for integrated layout design of planar multi-component systems using moving morphable bars, Comput. Methods Appl. Mech. Engrg. 342 (2018) 46–70, http://dx.doi.org/10.1016/j.cma.2018.07.032.
[57] R.D. Cook, D.S. Malkus, M.E. Plesha, R.J. Witt, Concepts and Applications of Finite Element Analysis, fourth ed., Wiley, 2001.
[58] L.V. Gibiansky, O. Sigmund, Multiphase composites with extremal bulk modulus, J. Mech. Phys. Solids 48 (3) (2000) 461–498, http://dx.doi.org/10.1016/s0022-5096(99)00043-5.
[59] X. Wang, K. Long, Z. Meng, B. Yu, C. Cheng, Explicit multi-material topology optimization embedded with variable-size movable holes using moving morphable bars, Eng. Optim. 53 (7) (2021) 1212–1229, http://dx.doi.org/10.1080/0305215x.2020.1779710.
[60] K. Svanberg, The method of moving asymptotes—a new method for structural optimization, Internat. J. Numer. Methods Engrg. 24 (2) (1987) 359–373, http://dx.doi.org/10.1002/nme.1620240207.
[61] X. Wang, P. Hu, Z. Kang, Layout optimization of continuum structures embedded with movable components and holes simultaneously, Struct. Multidiscip. Optim. 61 (2) (2020) 555–573, http://dx.doi.org/10.1007/s00158-019-02378-5.
[62] P. Duysinx, M.P.B. e, Topology optimization of continuum structures with local stress constraints, Internat. J. Numer. Methods Engrg. 43 (8) (1998) 1453–1478, http://dx.doi.org/10.1002/(sici)1097-0207(19981230)43:8<1453::aid-nme480>3.0.co;2-2.
[63] E. Fancello, Topology optimization for minimum mass design considering local failure constraints and contact boundary conditions, Struct. Multidiscip. Optim. 32 (3) (2006) 229–240, http://dx.doi.org/10.1007/s00158-006-0019-9.
[64] A. Verbart, Topology Optimization with Stress Constraints (Ph.D. thesis), Delft University of Technology, 2015.
[65] K. Svanberg, MMA and GCMMA – two methods for nonlinear optimization, 2007, URL: https://people.kth.se/~krille/mmagcmma.pdf.
[66] Intel®, Developer reference for Intel® oneAPI Math Kernel Library for C, 2023, URL: https://www.intel.com/content/www/us/en/docs/onemkl/developer-reference-c/2024-0/overview.html, Toolkit downloaded using the Conda package manager, as instructed in https://www.intel.com/content/www/us/en/docs/oneapi/installation-guide-windows/2024-1/conda.html.
[67] O. Amir, N. Aage, B.S. Lazarov, On multigrid-CG for efficient topology optimization, Struct. Multidiscip. Optim. 49 (5) (2014) 815–829, http://dx.doi.org/10.1007/s00158-013-1015-5.
[68] E.A. Träff, A. Rydahl, S. Karlsson, O. Sigmund, N. Aage, Simple and efficient GPU accelerated topology optimisation: Codes and applications, Comput. Methods Appl. Mech. Engrg. 410 (2023) 116043, http://dx.doi.org/10.1016/j.cma.2023.116043.
[69] Y. Wang, Z. Luo, N. Zhang, Z. Kang, Topological shape optimization of microstructural metamaterials using a level set method, Comput. Mater. Sci. 87 (2014) 178–186, http://dx.doi.org/10.1016/j.commatsci.2014.02.006.